12-2017

Modeling Defect Evolution in Irradiated 800H using Cluster Dynamics

Andrew Nicholas Payant
University of Tennessee, apayant@vols.utk.edu

To the Graduate Council:

I am submitting herewith a thesis written by Andrew Nicholas Payant entitled "Modeling Defect Evolution in Irradiated 800H using Cluster Dynamics." I have examined the final electronic copy of this thesis for form and content and recommend that it be accepted in partial fulfillment of the requirements for the degree of Master of Science, with a major in Nuclear Engineering.

Brian D. Wirth, Major Professor

We have read this thesis and recommend its acceptance:

Maik K. Lang, Steven J. Zinkle

Accepted for the Council:
Carolyn R. Hodges

Vice Provost and Dean of the Graduate School

(Original signatures are on file with official student records.)

Modeling Defect Evolution in Irradiated 800H using Cluster Dynamics

A Thesis Presented for the

Master of Science

Degree

The University of Tennessee, Knoxville

Andrew Nicholas Payant

December 2017

Acknowledgments

I would like to express my thanks to Dr. Brian Wirth and Dr. Aaron Kohnert for their advice and guidance in my graduate research and for pushing me to strive for excellence in my work. I would also like to thank Dr. Steven Zinkle and Dr. Maik Lang for being on my committee and giving me much of the knowledge I gained in my graduate studies. Lastly, I would like to thank all of my family and friends. Without their loving support through the years, this work would not have be possible.

Abstract

A reaction-diffusion reaction rate theory based cluster dynamics was used to model the microstructure evolution of Alloy 800H under conditions similar to that of current and proposed nuclear reactors. The predicted interstitial and vacancy faulted loop densities grew orders of magnitude larger than experimentally measured in similar environments. The large calculated densities were determined to result from the over-nucleation of faulted loops directly generated by irradiation. In order to reduce the number densities, an additional reaction term is proposed that would approximate the enhanced recombination and reduced damage production caused by the damage cascade volume overlapping with the physical volume of defect clusters. To correctly parameterize the modified recombination and production terms, molecular dynamics simulations need to be performed to provide a computational database on the effects of a cascade overlapping with pre-existing defects.

Table of Contents

List of Figures

Chapter 1

Introduction

As nations aim to reduce their carbon footprint and develop their infrastructure, the need for safe and reliable nuclear energy has steadily increased. With current goals set to double total power generation of the entire globe by 2050, the capacity of nuclear reactors needs to increase from 400 GW to 1 TW, or more [1]. In order to meet this demand, designs for the next generation of nuclear reactors (Generation IV) are being proposed. These Generation IV reactors will have much longer operating lifetimes and have higher thermal efficiencies resulting from high coolant temperatures. In addition to adding new reactors, most of the current fleet of nuclear reactors are seeking to extend their operating licenses beyond the current 60 year licenses [2, 3, 4]. A key requirement in extending operation limits of current reactors, and in planning for new plants, is assuring that the degradation and aging that the components experience during operation is within safety standards [3]. In fission reactors, materials are exposed to highly energetic particles that produce a wide range of degradation phenomena. Depending on the temperature and particular material, these degradations include enhanced creep, volumetric swelling, loss of ductility, irradiation assisted stress corrosion cracking (IASCC), radiation induced precipitation, and many more [4, 5, 6]. These phenomena increase the frequency of shutdowns required for maintenance when components fail and put tight limits on reactors' design and operations. When considering current designs for Generation IV reactors, the need for materials where the irradiation degradation is less severe is strong since the operating conditions for all the future design span a much wider temperature range and much higher doses compared to current reactors. A quick summary

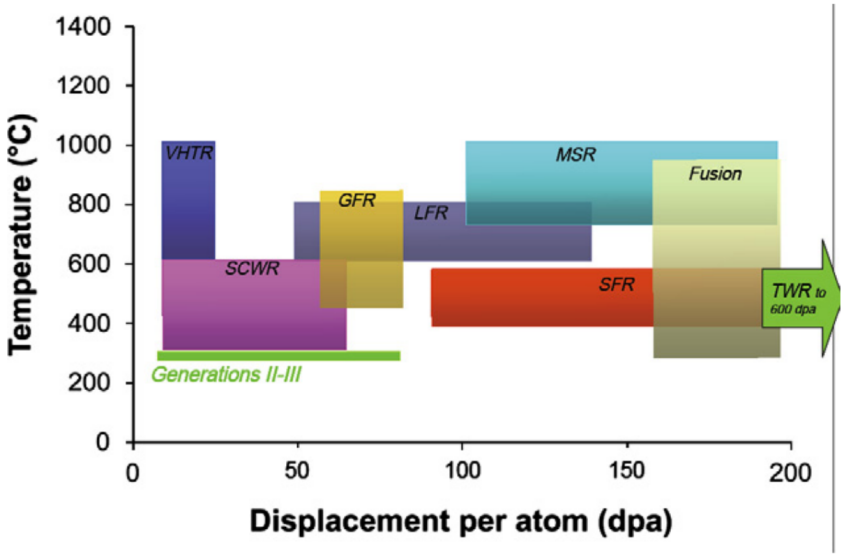

Figure 1.1: The operating temperatures and doses expected for materials in various Generation IV designs. Reproduced from Ref. [6]. Most designs have materials to a greater total dose compared to our current Generation II and III reactors. All have higher operation temperatures.

of the operational conditions for some Generation IV reactors is shown in Figure 1.1 A major consideration when investigating candidate materials for future nuclear reactors is whether performance will be maintained under irradiation. High corrosion resistance, high creep and yield strength, and good ductility are desired for use in both the in-core and out-of-core components, like heat exchangers and piping. As an example, stress corrosion cracking (SCC) is a failure mode for many materials where corrosion weakens the material such that relatively low tensile stresses causes cracks to propagate. Ni-rich alloys tend to have corrosion resistant properties, particularly in the high temperature regions being considered for Generation IV plants. Austenitic stainless steels (SS), in addition to being nickel rich, have good corrosion resistance due to the chromium forming a protective oxide layer on the steel/coolant interface. Aside from corrosion resistance, resistance to void swelling and phase instability is also essential to the long term integrity of the steel. In currently operating reactors, a majority of the core support structures are made of austenitic steels like Type 306 and 316 SS [6]. The ability to predict the behavior of those steels as reactors seek license extensions is critical for determining what operation conditions are acceptable. In order to

improve the overall performance of current and future reactors, it is necessary to have a thorough physical understanding of the how the materials behave within a harsh radiation environment as well as the mechanisms that cause the accelerated degradation.

1.1 Stainless steels in irradiation environments

A majority of core structural components and secondary side equipment such as piping is made out of austenitic steels. Since austenitic stainless steels, like 316 and 304, are so prevalent in the current fleet, there is a great deal of literature investigating how these steels degrade in a large range of radiation environments. One major issue that austenitic stainless steels are particularly susceptible to is void swelling. An example of the void swelling experienced by 304 SS under neutron irradiation is shown in Figure 1.2. The figure shows a transmission electron microscopy (TEM) image of 304 after being irradiated at 595°C, which corresponds to about 42% of the melting temperature of 304 SS. The figure also shows that the large voids dominate the microstructure of the steel after being irradiated to roughly 14 dpa (displacements per atom) at those high temperatures. As the defects produced in damage cascades diffuse through the material, the vacancies (and interstitials) can cluster together into larger defects. One such large cluster for vacancies is an approximately spherical cavity that adds extra volume to the lattice. These cavities, sometimes stabilized by the helium produced through nuclear reactions, harden the material and are a signature of large amounts of dimension change. In Figure 1.2, with the given densities and average void diameter of 3×10^{20} $m^{-3}$and 38 nm, the swelling the material experiences corresponds to a 0.8% increase in volume.

Void swelling is sensitive to the radiation environment, in particular the temperature of the material. The metal temperature typically needs to be around 45% of its melting temperature for void swelling to occur. At temperatures greater than 0.45 T_m, vacancies can diffuse the lattice easily, but more importantly, vacancies trapped in in small vacancy clusters can disassociate and produce a super-saturation of mobile vacancies. If the temperatures are too low, any cavities generated cannot grow to large size because a large number of vacancies are trapped in small clusters. If temperatures exceed 0.6 T_m, then the cavities also begin

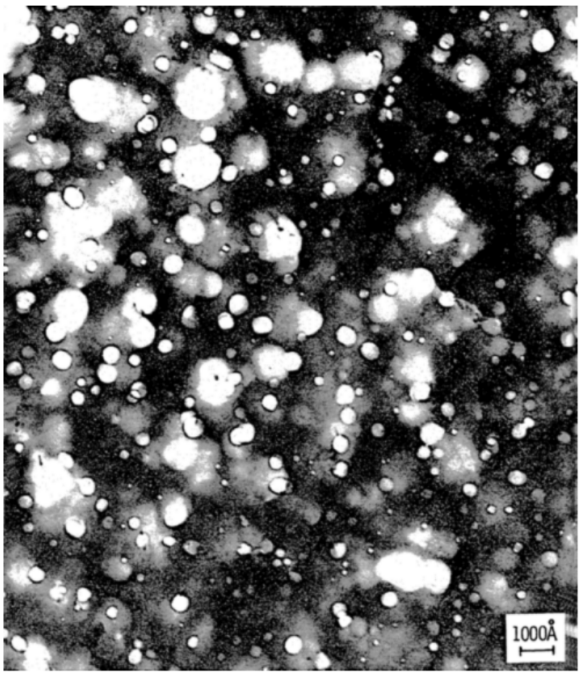

Figure 1.2: A TEM image of 304 SS microstructure when irradiated with neutrons up to a fluence of 3×10^{22} n $\cdot$ cm^{-2} (roughly 14 dpa) at 595°C by Ref. [7]. The cavity density for this sample was 3×10^{14} cm^{-3} with an average diameter of 380Å.

to disassociate. By designing materials that impede the flux of vacancies to cavities, either by limiting the vacancy mobility or introducing sinks for vacancies, the amount of swelling can be reduced. There is some evidence that the addition of nickel to austenitic stainless steel does limit the amount of swelling, but austenitics still experience large amounts of void swelling relative to ferritic steels under similar conditions [6, 7].

Cavities, as well as other large defect clusters configurations, are also associated with the increased yield strength and reduced ductility that is observed under irradiation. These alternate geometries, often platelets of vacancies or self-interstitial atoms (called dislocation loops), impede the motion of dislocations in response to applied stress and are often found in irradiated austenitic steels. These defect loops can be of vacancy or interstitial nature, and tend to be observed at lower irradiation temperatures. At high temperatures, the loops can shrink and be removed by the thermal emission of single vacancies in the case of a vacancy loop, or grow large enough to connect with dislocation networks for the case of large interstitial loops. The large defect loops greater than 10 nm in size seen in austenitic steels such as 316 are often interstitial in nature and have ($\vec{b} = \frac{a_0}{3}\langle 111 \rangle$) making them Faulted (also

called Frank loops). These defect loops tend to be found in densities near 10^{22} m^{-3} at doses near 1 dpa and grow in size with increasing dose for most austenitic stainless steels [8, 9].

Another degradation phenomena that significantly impacts the performance of the steel is the formation of precipitates and radiation-induced segregation. In short, the flux of defects produced in a damage cascade to various sinks causes the elements in the steel to segregate. In stainless steels, this depletes the chromium content around grain boundaries, weakening them and decreasing the oxidation resistance of the boundary. This segregation often gets severe enough that different phases begin to precipitate out of the steel. Which precipitates form and at what doses they appear is highly sensitive to temperature and the chemical composition of the steel. Some common precipitates that are seen in austenitic stainless steels are chromium rich carbides like $M_{23}C_6$ or intermetallics like the chromium and molybdenum rich σ-phase [10].

The large defect clusters we have discussed thus far do change the macroscopic properties of a material in an additional way. Under irradiation, steels experience a increase in yield and tensile strength and, for FCC steels specifically, a decrease in fracture toughness. The changes in microstructure when irradiated can be related to the increase of strength through two models, the dispersed barrier model and the Friedel-Kroupa-Hirsch model [11]. In both models, the large defects impede the movements of dislocations that are associated with a material deforming resulting in a increase strength (hardening). In addition to loops and precipitates hardening alloys, large precipitates are thought to have an enhancing effect on the growth of cavities, as well as serving as initiation sites for stress corrosion cracking [12, 13].

1.2 800H in Irradiation environments

800H is a nickel-rich austenitic alloy that is a candidate material for future reactors. Its full chemical composition given by Ref. [14] is listed in table 1.1. The alloy is being considered for the heat exchanger and steam generators, as well as in some components in Generation IV reactor designs. 800H is the only candidate material that has been AMSE qualified for nuclear applications up to 760°C. Prior to irradiation, the microstructure of 800H should

Table 1.1: Chemical composition of Alloy 800H in weight percent. Alloy 800H has the same composition as Alloy 800 but 800H is annealed at 1150°C instead of 980°C and has a more restricted carbon content. Values reproduced from Ref. [14].

Composition	wt %
Nickel	30.0-35.0
Chromium	19.0-23.0
Iron	39.5 min.
Carbon	0.05-0.10
Manganese	1.50 max.
Sulfur	0.015 max.
Silicon	1.0 max.
Copper	0.75 max.
Aluminum	0.15-0.6
Titanium	0.15-0.6

contain precipitates that strengthen the material. Ti-rich precipitates that are on average 500 nm in size have been observed by Ref. [15] but the number densities of such particles was was not reported. In other samples examined in Ref. [16], no preexisting precipitates were observed in 800H. This means that precipitates are normally present in 800H, but are typically of very low number densities. Preexisting dislocation networks with densities near 4×10^{13} m^{-2} in Ref. [15]. 800H has an average grain of size ¡60 μm, and considerable effort has gone toward engineering the grain boundaries to lower energy configurations to reduce the impact of radiation induced segregation [17, 18].

Along with SCC, void swelling is a major concern for alloys with austenitic crystal structure and should be worsened further by helium generation due to nickel. There is some evidence that the addition of nickel mitigates void swelling but the swelling for behavior is still severe compared to other alloys [20]. Alloy 800, which has less restricted carbon concentrations and a lower temperature heat treatment, exhibited up to 41% swelling for extremely high doses as shown in Figure 1.3. Compared to the other austenitic alloys irradiated in the experiment, alloy 800 exhibited swelling that was four times larger than the other nickel-rich alloys that were irradiated under similar conditions.

After 3 dpa from neutron irradiation at 500°C, Ref. [21] reported densities of 2.85×10^{22} m^{-3} and 1.46×10^{22} m^{-3} for defect loops and $Ni_3(Ti, Al)$ (called γ' precipitates), respectively. The average sizes were 6.0 nm for the Frank loops and 2.2 nm for the

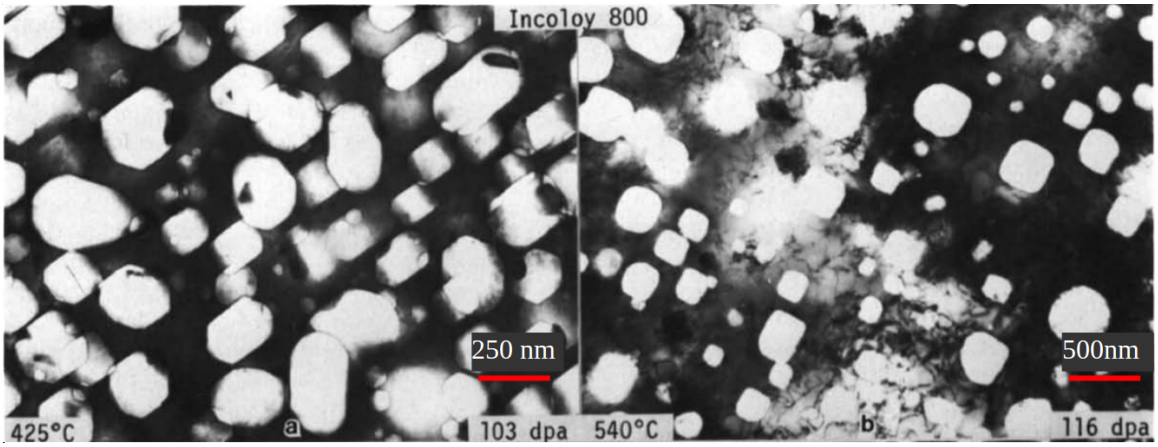

Figure 1.3: A TEM image of the microstructure of austenitic alloy 800 when irradiated with neutrons up to 103 and 116 dpa by Ref. [19]. The high density of large cavities correspond to swelling of 12.0% and 41.1%, respectively.

precipitates. Cavities were also seen in the same irradiation conditions with densities of 1.9×10^{22} m^{-3} and average diameter of 3.3 nm. At a slightly lower dose of 1.3 dpa, Ref. [15] also saw a distribution for 'micro-voids' with $\rho = 2.5 \times 10^{20}$ m^{-3} and average diameter of 3.6 nm. The microstructure of 800H was determined to be dominated by large precipitates such as γ' and Cr-rich $M_{23}C_6$ that had average sizes of 34.7 and 34.2 nm and $\rho = 3.4 \times 10^{20}$ m^{-3} and $\rho = 5.5 \times 10^{20}$ m^{-3}, respectively.

While there are numerous experimental papers describing the response of alloy 800H to different irradiation environments, there is a lack of work on predictive modeling of the microstructure evolution. The goal of this work is to build the beginning of a model describing the evolution of the microstructure of Alloy 800H under irradiation.

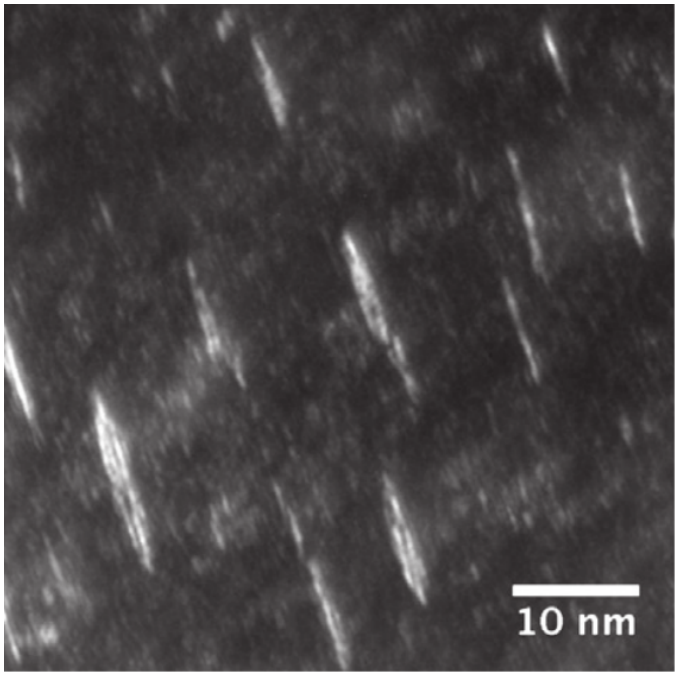

Figure 1.4: A TEM image of 800H neutron irradiated microstructure performed by Ref. [21]. The sample was irradiated at 500° up to 3 dpa. The corresponding Frank loop number density is $2.85 \times 10^{22}\ m^{-3}$

Chapter 2

Methods

2.1 Cluster dynamics

Mean-field cluster dynamics models, which are an extension of the traditional reaction-diffusion based rate theory [9, 22, 23, 24] are powerful tools for predicting the microstructure response under irradiation. By expanding the number of point defect balance equations to describe every possible cluster type and size, as well as the possible interactions between them, one derives a series of equations of the form of equation 2.1.

$$\frac{dC_i(x,t)}{dt} = \nabla(D_i(x)\nabla C_i(x,t)) + g_i(x) + D_i(x)k_i(x)^2 C_i(x,t) + R_i(\mathbf{C}(x,t)) \tag{2.1}$$

Equation 2.1 describes the time evolution of the concentration of a defect of size i. The first term on the right hand side denotes the spatial diffusion of the clusters. The second term describes the rate of generation of the defects. For materials being exposed to irradiation, g_i describes the rate at which defects of size i are created and survive the initial recombination stage of cascade evolution, which typically lasts on the order of picoseconds. The third term describes the loss of defects to sinks. The sinks examined consist of grain boundaries and precipitates in the material. The final term on the right hand side represents the sum of all defect cluster reactions that contribute to increasing and decreasing the population of clusters of size i. A more expanded version of $R_i(\mathbf{C})$ is shown in equation 2.2.

$$R_i(C) = \underbrace{\sum_{j+k\to i} k^+_{j,k} C_j C_k}_{\text{Generation due to reactions into } i} - \overbrace{\sum_{i+j\to k} k^+_{i,j} C_i C_j}^{\text{Loss due to reactions out of } i} + \underbrace{\sum_{k\to i+j} k^-_{k\to i,j} C_k}_{\text{Generation due to emission into } i} - \overbrace{\sum_{i\to j+k} k^-_{i\to j,k} C_i}^{\text{Loss due to emission out of } i} \tag{2.2}$$

There are two type of reactions that occur that would effect number density, a defect-defect interaction or an emission of base defect that together form the larger cluster, called a monomer. The first term in equation 2.2 represents all the interactions between clusters of sizes j and k that react to make a cluster of size i. The rate at which these reactions occur depend on the concentration of the two reacting clusters C_j and C_k and some reaction rate constant $k^+_{j,k}$ that depends on the mobility and geometry of the two clusters. Since cluster i can also react with defects, there is an additional summation that includes all interactions of cluster i and cluster j. The third and forth term in equation 2.2 are the contribution of clusters k emitting a cluster of size i and a cluster i emitting a cluster of size j, respectively. $k^-_{i\to j,k}$ is the reaction rate constant that describes the rate at which clusters of size i emit its associated monomer. This dissociation rate is usually a thermal mechanism, and is proportional to the $\exp(-\Delta E/kT)$ where ΔE is the difference in binding energy of the original defect and larger daughter defect, T is the absolute temperature, and k is the Boltzmann constant. Which specific interactions are allowed and how the geometries of each defect changes the rates of specific reactions means that cluster dynamics needs to have at least a nanoscale understanding of defect-defect interactions. Since equation 2.2 depends on the entire concentration vector, the reaction term couples together the numerous differential equations. This coupling requires that some numerical methods are implemented to find the correct value of each C_i at every timestep that would fit the set of differential equations. At each timestep, the terms in equation 2.1 are evaluated for each cluster population. The net change in concentration for each cluster population is then applied to each C_i, evolving all defect populations simultaneously. One benefit of cluster dynamics models is that defect clusters of any size can be generated directly. This allows for a more accurate defect generation distribution where large defects can be nucleated directly through cascades instead of growing from interactions with smaller defects. Another benefit is that large defects can essentially act as sinks that can vary in strength as the cluster number

density grows or shrinks. Since the large defects can be removed from the system through recombination, the associated defect removal through reaction diffusion interactions is not a constant through time. Those diffusion reactions depend on the concentration of the two defects and the unique reaction rate coefficient for each combination of defect $k^+_{i,j}$. Each $k^+_{i,j}$, first derived by Ref. [25], take the form of equation 2.3.

$$k^+_{i,j} = 4\pi(D_i + D_j)(r_i + r_j + r_0) \tag{2.3}$$

Equation 2.3 assumes that the absorbing defect has a spherical geometry and includes the mobility of each cluster, in so depends on the diffusion coefficient of each reacting cluster D_i, D_j. The reaction rate also depends on the radius of the interaction volume, which is the sum of the size of both defectsr_i, r_j and the recombination distance r_0.

Normally, if the number of equations is large, solving these equations can become too computationally expensive. As an example, if one wishes to simulate the effects of helium generation on the development of loops and cavities up to a maximum cluster size of N, the number of equations increases by a factor of N due to the fact that each equation describing a clean vacancy cluster population now has a wide range of helium atoms concentrations inside that cluster as well each of which need an individual equation 2.1. Another example where cluster dynamics can be computationally expensive is if the defect cluster sizes grow too large. Considering voids that grow up to 30 nanometers in diameter requires 10^6 equations to describe the vacancy populations that clustered into that large size. SPICES (Spatially-resolved Inter-scale Cluster Evolution System), developed by Aaron A Kohnert and Brian D. Wirth [24], utilizes a grouping scheme to reduce the total number of equations significantly, allowing for large-sized defect populations to be modeled. SPICES also includes a more generalized form of $k_{i,j}$ that can be applied for loop geometries shown in equations 2.4 through 2.8.

$$k^2_{L,j} = D_j[pZ_s + (1-p)Z_L] \tag{2.4}$$

$$Z_s = 4\pi(r_L + r_j + r_{core}) \tag{2.5}$$

$$Z_L = 4\pi^2 r_L / log(1 + 8r_L/(r_j + r_{core})) \tag{2.6}$$

$$p = \frac{1}{1 + (r_L/(r_j + r_{core}))^2} \tag{2.7}$$

Equation 2.4 describes the sink strength of defects with loop geometries as a superposition of spherical sink strength and toroidal sink strength with the spherical term largest at small loop radius. Z_s is the spherical contribution to the sink strength, which depends on the radius of the loop r_L, the size of the diffusing defect r_j, and the defect capture radius r_{core}. Similarly, the loop nature of the sink strength is represented by equation 2.6 and also depends on r_L, r_j, and r_{core}. p, described in equation 2.7, represents to what degree the defect loop appears as a spherical sink to the diffusing defect. Equation 2.4 describes the sink strength of the loop, which is a property of how strongly defects are attracted to the absorbing defect. The sink strength can be converted to a reaction rate constant through equation 2.8, so that the expression for loop sink strength to can be considered a dynamic sink of the system since the loop concentration C_j will evolve with irradiation.

$$k^+_{i,j} = D_i k^2_{i,j}/C_j \tag{2.8}$$

2.1.1 FCC Defects Cluster Configurations

There are several possible defect cluster types in an fcc crystal structure. A perfect dislocation loop is a plane of interstitials or vacancies ($\vec{b} = \frac{a_0}{2}\langle 110\rangle$) that can move through the crystal lattice (termed as glissile). Perfect loops have slip planes on the $\{111\}$ planes. Perfect loops can disassociate by a reaction described in equation 2.9 into two partial dislocations called Shockley partials.

$$\frac{a_0}{2}\langle 110\rangle \rightarrow \frac{a_0}{6}\langle 211\rangle + \frac{a_0}{6}\langle 12\bar{1}\rangle \tag{2.9}$$

The Shockley partials have $\vec{b} = \frac{a_0}{6}\langle 112\rangle$ which bound a stacking fault. Shockley partials form because the mechanism by which perfect loops glide energetically prefers moving from one stacking fault sequence to the next rather than directly moving with the Burgers vector, shown in Figure 2.1. Since a perfect loop dissociating into Shockley partials leads to movement by changing stacking fault, the perfect loop becomes an 'extended' dislocation,

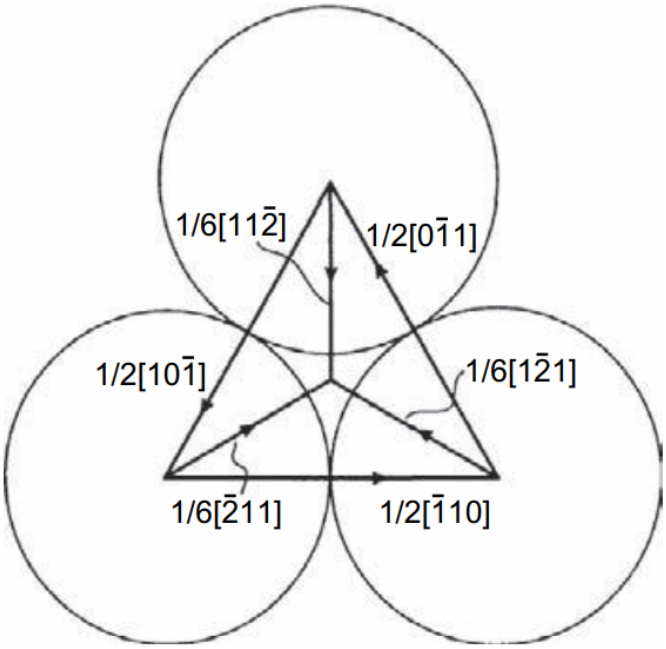

Figure 2.1: A representation, reproduced from Ref. [26], of how perfect loops can be decomposed into two smaller displacements which are Shockley partials in the (111) plane.

with the first Shockley partial creating a stacking fault and the second one removing it. The distance of separation between the two Shockley partials is determined by balancing the repulsive force of the two dislocations on each other and the attractive force caused by the stacking faults, leading to equation 2.10.

$$d = \frac{Gb^2}{4\pi\gamma} \tag{2.10}$$

In Equation 2.10, the distance between Shockley partials dislocations depends on the shear modulus G, the Burgers vector for the Shockley partial b and the stacking fault energy γ. Shockley partials can also react with faulted loops in a unfaulting reaction that transforms them into perfect dislocations [26]. Faulted (Frank) loops ($\vec{b} = \frac{a_0}{3}\langle 111\rangle$) are an interruption of the stacking order in the $\{111\}$ plane. Faulted loops can either be an inserted plane of atoms (interstitial loop or extrinsic) or a missing plane of atoms (vacancy loop or intrinsic) and are not mobile (called sessile). Another type of defect cluster is a stacking fault tetrahedron (SFTs), which are 3-D vacancy stacking faults cluster bound by $\vec{b} = \frac{a_0}{6}\langle 110\rangle$ type dislocations,

which are referred to as stair-rod partial dislocations, and are possible because the close-packed planes of FCC lattice are the {111} planes which form a tetrahedron. While SFTs are often seen in simple metals under irradiation, SFTs are generally not seen in significant numbers in austenitic steels or alloys [27].

In addition to those defect clusters, cavities can be created if the concentration of mobile vacancies is high enough. The formation of cavities can be aided by noble gases that stabilize the small nucleation sites. In particular for 800H, a nickel rich alloy, helium is produced under neutron irradiation through the following reaction:$^{58}\mathrm{Ni}(n,\gamma)^{59}\mathrm{Ni}(n,\alpha)^{56}\mathrm{Fe}$. As mentioned previously, precipitates can form in metals during irradiation. For 800H, these precipitates often are chromium rich carbides (such as $\mathrm{M_{23}C_6}$) or nickel based intermetallics γ' phase. While these precipitates can act as defect sinks and reduce the total concentration of defects, they also can act as nucleation sites for the larger sized defect clusters. Precipitates act as barriers to dislocation movement, and are associated with a increase in yield strength [11]. In this work, we only consider precipitates as static sinks for defects present prior to irradiation to simplify the calculations.

2.1.2 Vacancy Cluster Binding Energies

In order to take into account the emission of single vacancies or self-interstitial atoms from large clusters, we need to calculate the binding energy of the different possible defect geometries. In work done by Ref. [28], using elastic continuum expressions, the stability of large vacancy defects was used to determine which types of vacancy defects would be the most energetically favorable. Using the same equations, we generated how stable each cluster is as a function of size. Equation 2.11 represents the formation energy for a faulted vacancy loop, and depends on the stacking fault energy of the loop, which is the area of the loop πR^2 and the stacking fault energy γ. It also depends on the ratio between the Burgers vectors of faulted loops b_F over the Burgers vector of the perfect loop b and the energy stored in the perfect loop E_p.

$$E_F = \frac{b_F^2}{b^2} E_p + \pi R^2 \gamma \tag{2.11}$$

The formation energy for a perfect vacancy loop, shown in equation 2.12, depends on the Burgers vector of the perfect loop b, the shear modulus G, the Poisson ratio ν, the radius of the loop R, and the dislocation core radius ϵ. The functions $F(K)$ and $E(K)$ are elliptic integrals of the first and second kind, respectively.

$$E_p = \frac{Gb^2}{2(1-\nu)}\{2R + (2R-\epsilon)[(1-0.5K^2)F(K) - E(K)]\} \tag{2.12}$$

where

$$K^2 = \frac{4R(R-\epsilon)}{(2R-\epsilon)^2}$$

Equation 2.13 describes the formation energy for a clean void. The binding energy of the void only depends on the surface area of the void $4\pi R_v^2$ and the surface energy for that metal Γ. The inclusion of the $0.8/(N+2)$ term is an empirical addition that accounts for deviations in small void binding energy.

$$E_v = 4\pi R_v^2 \Gamma\big(1 - \frac{0.8}{N+2}\big) \tag{2.13}$$

For stacking fault tetrahedra, a defect that is unique to fcc materials, the formation energy is given by equation 2.14. Like the faulted loop binding energy, the SFT binding energy has a term associated with the produced stacking faults and the strain field produced by the six segments of stair-rod dislocation, both depending on the edge length of the tetrahedron L.

$$E_{SFT} = \frac{Gb^2 L}{6\pi(1-\nu)}\{ln\frac{4L}{b} + 1.017 + 0.97\nu\} + \sqrt{3}L^2\gamma \tag{2.14}$$

By using these equations and the appropriate parameters of 800H, the formation energetics of defect clusters can be determined, along with the lowest energy configuration. We used $\nu = 0.36$, $G = 65$ GPa from the report given by Ref. [14] for alloy 800 at 350°C. For the surface energy Γ, we used $\Gamma = 2.1\text{J/m}^2$ the average of calculated values for a 50Ni-50Fe and 25Ni-75Fe binary alloys from Ref. [29] as an approximation for 800H. For the stacking fault energy γ, we used $\gamma = 84\text{mJ/m}^2$ as the approximate value taken by using the tabulations of Fe-20Cr-30Ni steels in Ref. [30] and from the experimental values from Refs. [31] and [32] of

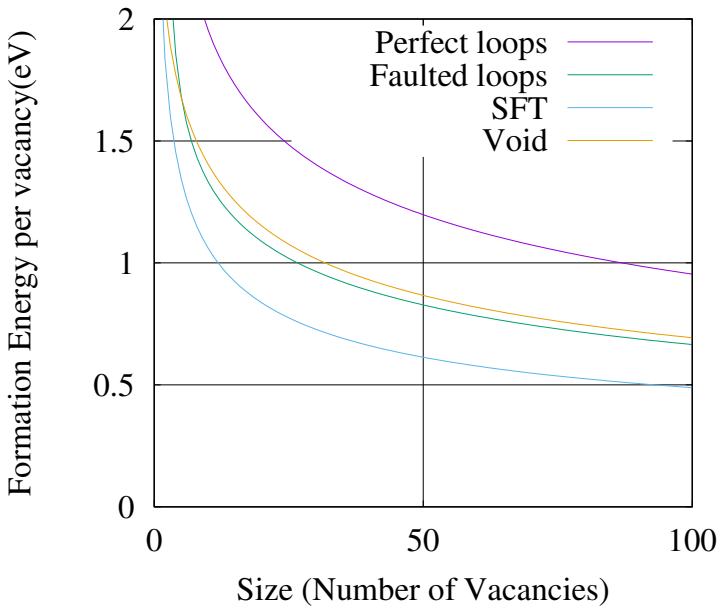

Figure 2.2: The formation energy for each vacancy defect geometry per vacancy calculated for 800H using equations from Ref. [28]. Although Stacking Fault Tetrahedra are the most stable of the cluster geometries, they have not been included in this modeling effort since they are not seen in austenitic steels.

similar composition alloys to 800H. Figure 2.2 plots the energy of formation of the vacancy cluster per vacancy in that cluster as a function of cluster size for the appropriate values.

It is worth noting that based on Figure 2.2, SFTs should be the most stable and prevalent defect in 800H. However, since SFTs are not seen in 800H or austenitic steels in general, this defect cluster has not been included in this model for radiation defect evolution in alloy 800H. Since faulted loops are the next most stable configuration, we will assume that they are the defect geometry that large vacancy clusters are generated in. Another note is that vacancies in the perfect loop configuration are the most energetically unfavorable of the defect geometries by nearly 0.5 eV per vacancy. Because of this large difference, we assume perfect vacancy loops is negligible compared to the generation of the faulted configuration and can be ignored from the models.

In order to use these equations in SPICES, we fit equations 2.11 and 2.13 to a capillary emission law, described in equation 2.15, that describes the required energy to emit one

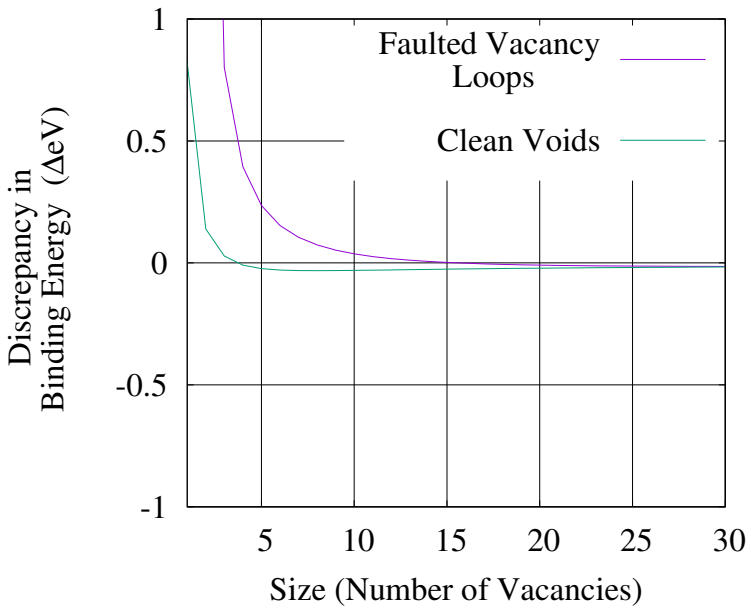

Figure 2.3: Shows the difference between the capillary law fit for the binding energy per number of vacancies compared to the continuum physics equation calculated by Ref. [28].

vacancy from the larger vacancy cluster.

$$E_b = E_1 - E_n(n^{2/3} - (n-1)^{2/3}) \tag{2.15}$$

In fitting the capillary law(s) to the continuum expressions, there are some discrepancies at small cluster size. Depending on the sign and magnitude of the discrepancy, this could result in a cluster that is artificially stable or unstable in our model. Figure 2.3 shows the discrepancy between the capillary law fit and the values as calculated using the continuum expressions for both clean voids and faulted loops. The difference is most significant for small number of vacancies ($\sim$5) and can exceed 0.5 eV. However, we define our defect types so that the fit equations only apply if the number of vacancies is greater than 6, so this difference can be ignored for our models.

2.1.3 Generation terms

We chose the g_i terms based on work performed by Ref. [33], where cascades were performed with 25 keV PKAs on copper at 300 K. We determined that copper was a suitable surrogate

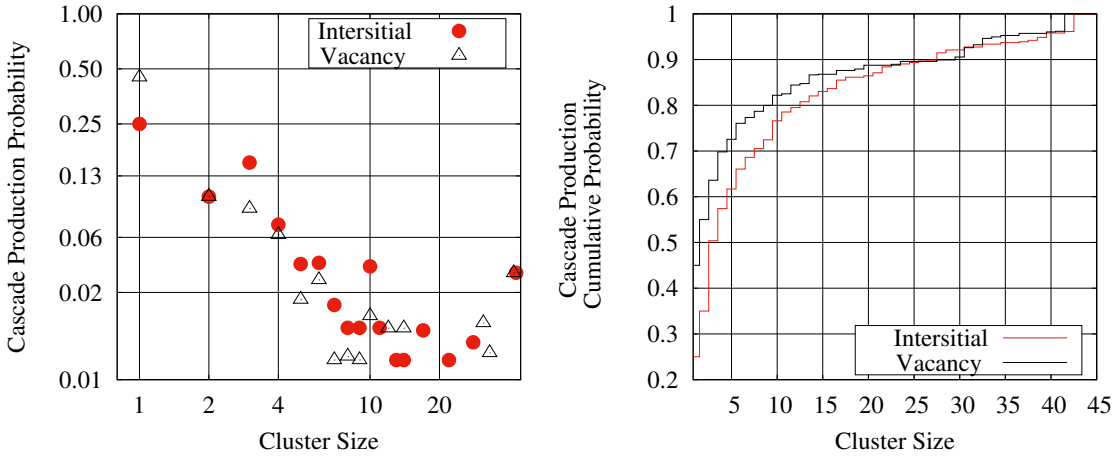

Figure 2.4: The size of defects produced in a 25 keV cascade in copper. On the left is the probability of a cascade producing a defect of that size. On the right is the cumulative of producing a defect of that size or smaller. Data reproduced from Ref. [33].

for our 800H models, since copper and 800H both have a face centered cubic crystal structure and many experimental and theoretical studies have been performed on defect behavior in copper. In the simulations performed by Ref. [33], 10 and 25 keV were simulated in a cell with 2 million copper atoms. At the higher PKA energy, a significant number of defects produced in the cascade have sizes greater than 20 at the end of the simulation. For both interstitials and vacancies, 6% of the defects have size greater than 41 defects in size. MD cascade simulations of copper often produce stacking fault tetrahedra (SFT) defects, which are not observed in austenitic stainless steels. We interpret SFT generation to be analogous to the generation large vacancy faulted loops of the same number of defects. For cluster dynamics, the generation term for defect sized i consists of what percentage of defects produced after a cascade are of size i and that probability is then scaled to be a volumetric defect creation rate. The probability distribution of the defect production rate is shown in Figure 2.4, which is extrapolated from Ref. [33]. Since a faulted loop is energetically more favorable for vacancies, we assume that all large defects produced directly in cascades were of loop geometry.

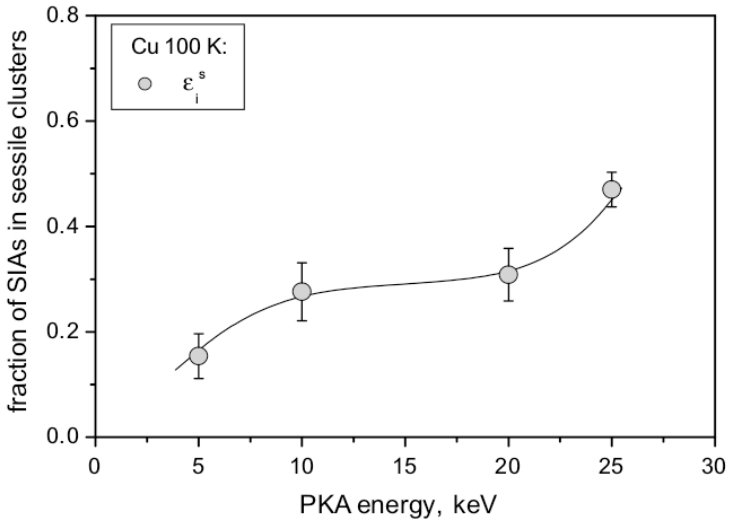

Figure 2.5: The fraction of interstitials defects produced into a sessile cluster as a function of PKA energy. Reproduced from Ref. [33].

2.1.4 Other Parameters

The various properties of the defects that we model for austenitic steels are given in Table 2.1. We separated the two different interstitial loop production terms by partitioning 80% of the loops produced in cascades to the glissile configuration (perfect) and the remainder 20% in the sessile configuration (faulted). This was determined from the MD cascade study from Ref. [33], for which the fraction of sessile SIA clusters observed as a function of PKA energy is shown in Figure 2.5. We assumed that the uncertainties around the fraction of SIA in sessile clusters was large enough, and copper was being used as surrogate for an austenitic nickel rich alloy that 20% in the sessile configuration was an appropriate approximation.

The migration energies described in Table 2.1 only apply to the point defect vacancy and self interstitial. The diffusivity of a defect of size i is calculated by $D_i = D_{0,i}\exp(-E_m/kT))$, where $D_{0,i}$ is the diffusion prefactor, T is the absolute temperature, k is the Boltzmann constant, and E_m is the migration energy of the defect. To insure that larger clusters' diffusivity reflects that larger defects are require higher temperatures to move, the diffusivity parameter for each defect has an additional $((n+1)^{-1})$ term that reduces the diffusivity prefactor. This is important for accurately modeling the movement of perfect loops, which are produced containing up to 45 interstitials. The diffusivity of the perfect loops for our

Table 2.1: A comparison of different definitions values for interstitials and vacancies used as inputs for cluster dynamics.

	Interstitial type	Vacancy type
Migration Energy	0.5 eV	1.3 eV
Formation Energy	3.4 eV	1.9 eV
Geometry	Sphere ($\leq$ 4) and Loop (>4)	Sphere (all sizes) and Loop (>6)
Mobility	For sphere and <110> loop geometry	Only sphere geometry with <6

model is a factor of 1/45 lower than for the single self interstitial atom, and this decreases the reaction rates constants when prefect loops are the diffusing species.

We also include an interstitial bias to sinks, including other large defect that are loops, of 20%. We also took the dislocation density found in 800H by Ref. [16] as a rough estimate for the nominal dislocation density of 800H prior to irradiation. We set that interstitial clusters with size of 5 or larger would be considered loop configurations with either perfect or Frank loops able to be formed through clustering. Since the formation energy of interstitials is so high compared to the formation energy of vacancies, we considered all interstitial clusters to be bound and not emit any single interstitials. We also start considering vacancies as either loops or voids once the cluster grows past 6 vacancies. While large vacancy clusters produced directly in cascades are always loops based on binding energies, both voids and and vacancy faulted loops can form from clustering of smaller vacancy groups.

Chapter 3

Results and Discussion

3.1 Preliminary results

While SPICES is capable of modeling the evolution of clusters on a spatially resolved scale, we reduced the problem to that of a bulk irradiation with no spatial dependence to minimize the calculation time. We also utilized the grouping technique described in Ref. [24], to reduce the total number of equations that are solved.

Using the parameters described in chapter 2 to describe 800H, we simulated neutron irradiation for the conditions shown in Table 3.1. The dose rate is 10^{-7}dpa/s and temperatures from 350°C to 650°C, corresponding to the irradiation experiments mentioned in chapter 1. We have simulated the neutron irradiation without helium to see the effects on the microstructure, as well as to reduce computation time. Note that by removing the production of helium from the simulation, vacancy faulted loops will be the dominate vacancy microstructure since the faulted loop configuration is energetically preferable to a clean void.

Table 3.1: A summary of the two base conditions used in our cluster dynamic simulations.

	Neutron Irradiation	MD Simulation Benchmark
Dose Rate	10^{-7}dpa/s	1.3×10^{7}dpa/s
Total Dose	10 dpa	0.065 dpa
Temperature	$623 - 923$K	300K
Intrinsic Sink Strength	10^{13} m^{-2}	0 m^{-2}

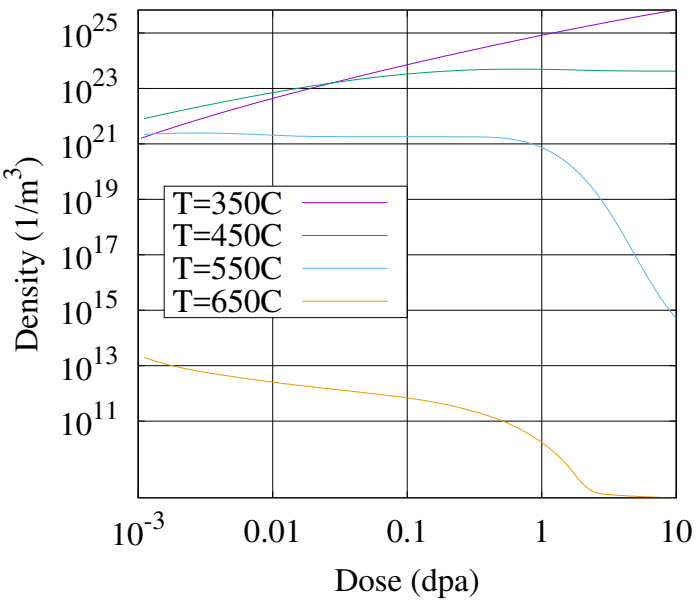

Figure 3.1: The vacancy faulted loop density as a function of dose and temperature using the neutron irradiation conditions described in Table 3.1. Note that the expected value around moderate doses (a few dpa) and temperatures should be 10^{22} m^{-3}.

It is important to note that perfect interstitial loops interact with either sinks or other defects, removing any perfect loops after being generated in cascade. Also the densities and average diameters were calculated by assuming that only loops with a minimum diameter of 2.5 nanometers count toward the measurable statistics of the populations since that is roughly the visibility limit of defects in TEM.

Figures 3.1 plots the calculated number densities for both vacancy faulted loops, as a function of dose (dpa) and irradiation temperature. As seen in Fig. 3.1, the faulted vacancy loop density increases nearly monotonically with dose at the two lower irradiation temperatures of 350° and 450°C, but exhibits a more complex dependence at higher temperatures. At a temperature of 550°C, the loop density is approximately constant until nearly 1 dpa, and then reduces by several orders of magnitude between and 10 dpa. At the two lowest irradiation temperatures, the faulted loop density exceed the experimentally measured values for similar conditions. We do see a significant reduction in vacancy loop density at 650°C, as compared to the lower irradiation temperatures. The melting temperature of 800H is around 1370°C and vacancy clusters begin to disassociate (Stage

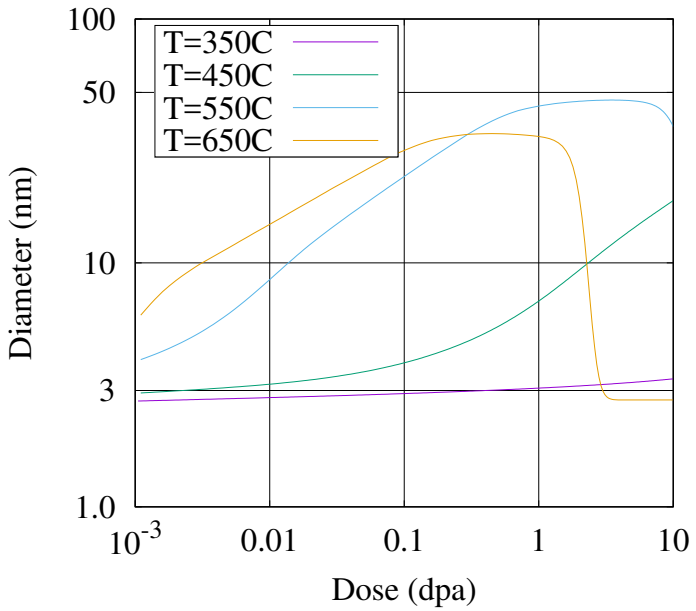

Figure 3.2: The average vacancy faulted loop diameter as a function of dose and temperature using the neutron irradiation conditions described in Table 3.1.

V) is near 0.45 of the melting temperature which is about 615°. At those temperatures, vacancy clusters will evaporate vacancies reducing in size to the point were they are no longer considered a loop, reducing the number density of loops as seen in Fig. 3.1. At lower temperatures evaporation still does occurs, but less frequently. The additional mobile vacancy population will go to the same sinks for defects they would normally: recombining with interstitials and interstitial-type dislocation loops, being removed by intrinsic sinks, or clustering with other vacancies.

Figure 3.2 plots the average vacancy loop diameter as a function of dose and temperature, and shows that the vacancy loop diameter generally increases with radiation dose, although this behavior seems to be highly sensitive to temperature which is likely the result of the evaporation of vacancy loops driving the growth. The vacancy loop evaporation also leads to a growth of the remaining vacancy loops as their densities decrease, as seen in Figure 3.2. This growth can also be seen when examining the size distribution of vacancy and interstitial faulted loop populations, respectively, which is shown in Figure 3.3. The large peak at small loop sizes shown in Fig. 3.3 is associated with: a combination of vacancy loops being generated at small sizes, loops being created with the combination of two vacancies,

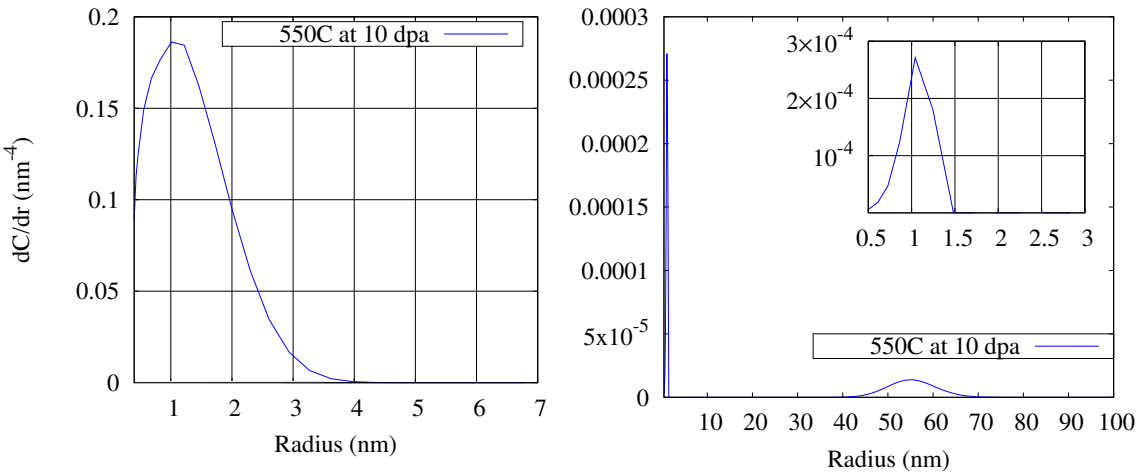

(a) Interstitial faulted loops

(b) Vacancy faulted loops

Figure 3.3: The distribution of both a) interstitial and b) vacancy faulted loops as a function of loop radius. The change in concentration was calculated using the neutron irradiation conditions described in Table 3.1. Both distributions were calculated at 10 dpa. The interstitial loop population is strongly peaked near the maximum cascade generation size. The vacancy loop population, once temperatures are sufficiently high, have a secondary peak at much larger sizes.

and larger vacancy loops absorbing interstitials or interstitial perfect loops. The second smaller peak shows a population of large loops absorbing migrating vacancy clusters and growing in size. As the production from disassociation beings to be mitigated by losses to sinks, the evaporation and associated additional flux of vacancies to other defects slow down the growth of the vacancy loops. We can see this at 550°C and 650°C in Figure 3.2 as a plateau in the average diameter with increasing dose. After the dose increases to a few dpa for 650°C and starting at 10 dpa for 550°C, the average size begins to decrease. This decrease to near generation size is due to interstitial loop densities becoming high enough to impact the flux of vacancies to the vacancy loops, causing their evaporation to reduce their size and density. We do not predict a significant reduction in the interstitial loop density or size at the sharp decrease in average vacancy loop size for 650°C. This can be explained by the very low densities or vacancy loops at that sharp drop do not produce enough vacancies to noticeably impact the interstitial loop size. At lower temperatures, the growth of vacancy loops only becomes significant at higher doses, near 0.1 dpa for 450°C and past 10 dpa for

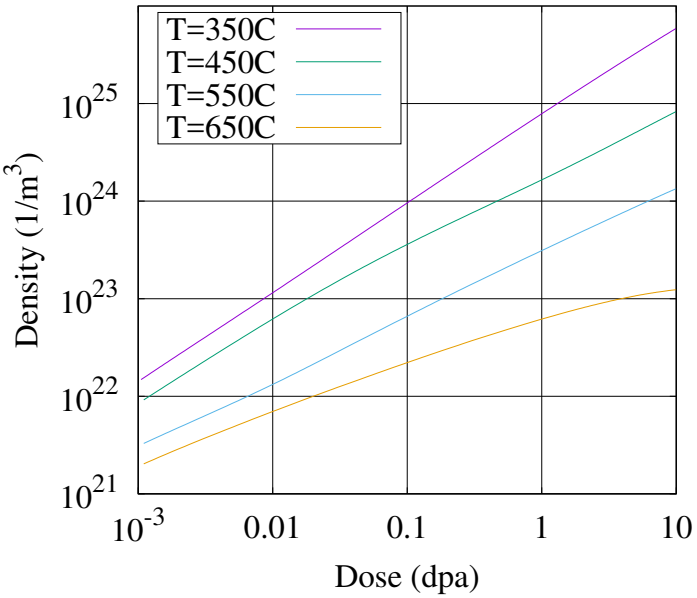

Figure 3.4: The interstitial faulted loop density as a function of dose and temperature using the neutron irradiation conditions described in Table 3.1. The predicted interstitial Frank loop densities are several orders of magnitudes higher that what has been observed for 800H in similar irradiation conditions.

350°C. This slowed growth is caused by the lower temperatures for which the vacancy loops are more stable, decreasing the number of free vacancies that would grow the loops.

In contrast, the interstitial faulted loops have a distribution similar to Fig. 3.3b at all temperatures, containing only a large peak at small sizes and then quickly fading to zero as loop sizes increase. This shows that even with large changes in temperature the interstitial loops are not growing beyond the size were they are being generated at in cascades, with the average diameter remaining near 3.5 nm, although there is some small growth in loop size as temperature increases. This is surprising since interstitials have much higher mobility than vacancies so we would expect there to be growth of interstitial faulted loops at lower temperatures even though there is not a strong additional source of interstitials with increasing temperature. The growth for interstitial loops should be near the same order of magnitude as for the vacancy faulted loops as a function of temperature. For vacancies, the growth between 350°C to 650°C corresponds to a factor of ten increase in size. For interstitial faulted loops, that number is closer to 6%. A much more troubling result, however, is the very high loop densities that are predicted at low temperatures shown in Figure 3.4. Particularly

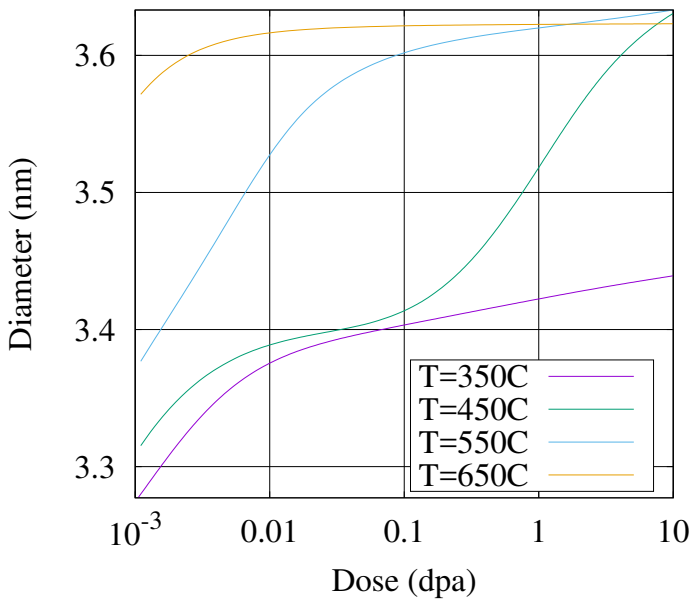

Figure 3.5: The average interstitial faulted loop diameter as a function of dose and temperature using the neutron irradiation conditions described in Table 3.1.

at 350°C, the number densities of both faulted loop populations increases with increasing dose, but neither change significantly in average size with the production of more interstitials and vacancies.

Based on the experimental results in 800H, as well as for other austenitic alloys, at a dose near 1 dpa one would expect that the loop density would be near 10^{22} m^{-3} for all faulted loops with sizes near 5 nm. We predict that the densities for both vacancy and interstitial loops would be more that 2 orders of magnitude larger than what has been observed in experiments with similar conditions. The evaporation of vacancy clusters does cause a decrease in interstitial loop density with temperature but the damage accumulation with increasing dose still drives the behavior of the interstitial loop densities. These large number densities of interstitial loops are likely the cause for the lack of loop growth that that we would expect with increasing dose, as the large number densities remove mobile defects averaged over the loop population. We do see the effects of the vacancy loop disassociation at high temperature acting as a small increase in the average diameter of interstitial faulted loops in Figure 3.5, but it is a minor effect. The decreasing vacancy loop density removes recombination sites for the mobile interstitials, causing an increase of mobile interstitial flux

to the interstitial faulted loops. The doses when interstitial loop diameters increase in Figure 3.5 do correspond to when the density of vacancy loops begins to decrease in Figure 3.1.

These extremely high densities, for low temperatures in particular, show no visible trend towards saturating as dose increases. The over-predicted high loop densities act essentially as artificial sinks for mobile defects and impact the growth other defects would experience if the loop densities were realistic. If we want to model the growth of cavities under a wide range of irradiation conditions, we need to be able to predict the microstructure accurately without the addition of helium, otherwise the predictions of cavity nucleation and growth will be in accurate.

Based on these high interstitial faulted loop number densities, something, or some parameter, in our model might be incorrect or some interaction that would lower the number densities is not being taken into account. Some parameters such as sink strength or migration energy of defects have a large impact on the calculation of reaction rates and therefore a strong influence on the evolution of the defect clusters. In order to investigate the underlying cause of these large loop densities, we performed a large number of simulations varying some key parameters to determine if the densities were sensitive to the variables that either vary from sample to sample or are hard to measure directly in experiment.

3.1.1 Sensitivity test: Sink Strength

Prior to irradiation, precipitates and dislocation networks often have sufficiently large size and densities to impact the total sink strength. Gan et al. [16] found a dislocation network density of 4×10^{13} m^{-2} but no precipitates in 800H. Special Metal Corporation states that precipitates such as titanium nitrides and chromium carbides are in the microstructure of 800H and are stable at all temperatures below the melting temperature [14]. A few Titanium rich precipitates were observed in Ref. [15] but no number densities were reported prior to irradiation. Because of the average density and size of precipitates of 800H prior to irradiation can vary from sample to sample, we might be under or over estimating the actual sink strength in our model. Grain boundaries or free surfaces do also act as sinks for mobile defects. But, the sink strength of the boundaries is proportional to the inverse of the size of

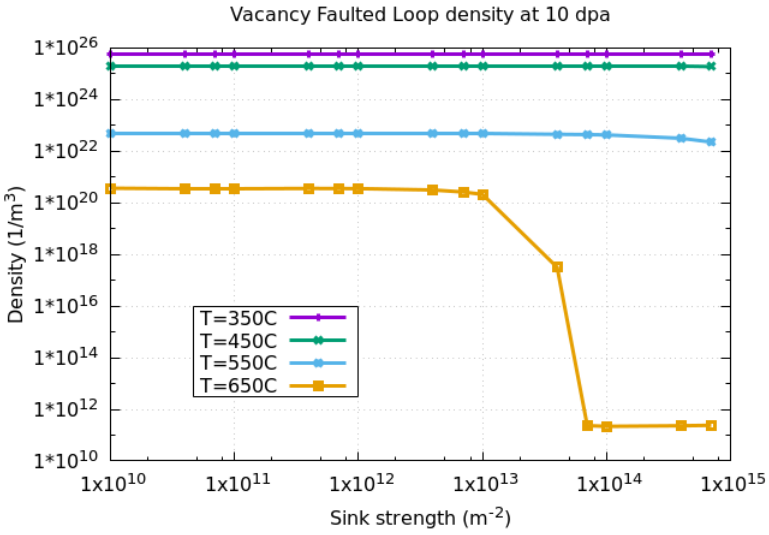

Figure 3.6: The concentration of vacancy faulted loops after 10 dpa as a function of intrinsic sink strength. The concentrations were calculated using the neutron irradiation conditions described in Table 3.1 except that the sink strength was varied from 10^{10} m^{-2} to 10^{15} m^{-2}.

the grain squared and for 800H the average grain size is too large to contribute significantly to the total sink strength compared to the dislocation networks or precipitates.

To determine how sensitive the predicted loop densities and sizes are to sink strengths, we varied the intrinsic sink strengths from 10^{10} m^{-2} to 10^{15} m^{-2} for the same neutron irradiated conditions. The densities of both vacancy and interstitial faulted loop types at a dose of 10 dpa are shown in figures 3.6 and 3.7, respectively as a function of sink strength.

The densities of the different faulted loops is relatively unchanged as a function of the sink strength variation from 10^{10} m^{-2} to 10^{15} m^{-2} with one major exception. For sink strengths greater than 10^{13} m^{-2}, a sharp drop in the density of vacancy faulted loops is observed at 650°C as well as a slight increase in the density of interstitial faulted loops under the same conditions. At 650°C, the vacancy loops are unstable and are disassociating into mobile vacancies. This caused the drop in density with increasing temperature for both types of loops as mentioned previously in describing the initial simulation results in Figs. 3.1-3.5. The growth we normally observe in faulted vacancy loops at high temperature is from the remaining vacancy loops absorbing the mobile vacancies that came from other vacancy loops. But, some of the freed mobile vacancies do cluster with other vacancies and reform loops. At sink strengths greater than 10^{13} m^{-2}, the liberated mobile vacancies go to the

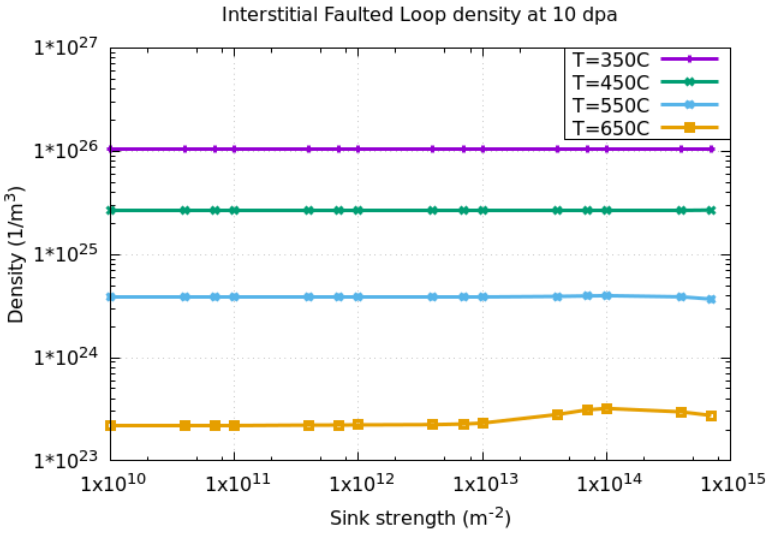

Figure 3.7: The concentration of interstitial faulted loops after 10 dpa as a function of intrinsic sink strength. The concentrations were calculated using the neutron irradiation conditions described in Table 3.1 except that the sink strength was varied from 10^{10} m^{-2} to 10^{15} m^{-2}.

sinks instead of the vacancy loops or other vacancy clusters, causing a decrease in vacancy loop density as sink strength increase. For the same reason, interstitial faulted loop density initially increases when most of the mobile vacancies freed from clusters at 650°C go to sinks instead of towards recombining with the interstitial loops and mobile interstitials. Aside from that deviation at high temperature and sink strengths, the high number densities at lower irradiation temperature are not significantly changed with the wide range of intrinsic sink strengths tested.

3.1.2 Sensitivity test: Migration Energy

The migration energy of the mobile vacancy and interstitial populations is one of the key variables in calculating the diffusivity D_i of a cluster size i which directly contributes to the rate of reactions through equation 2.3. The diffusivity of a defect relates to the migration energy by a $\exp(-E_m/kT)$), causing the thermal mobility of the defects to respond strongly to changes in migration energies. The migration energies for vacancies range from 0.5 to 1.5 eV and 0.1 to 0.7 eV for interstitials and depends on the crystal structure and chemical composition. Since all the reaction rates depend on the diffusivity of the mobile defects, we

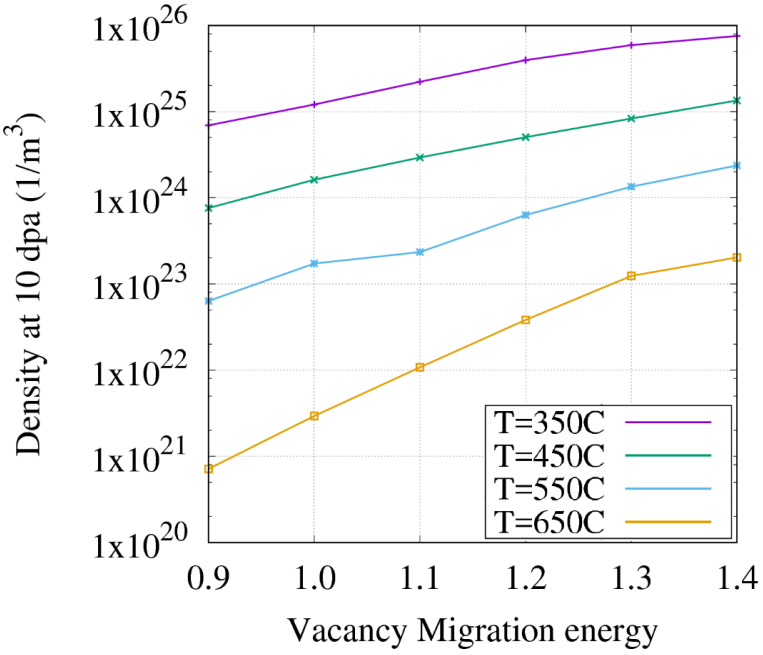

Figure 3.8: The concentration of interstitial faulted loops after 10 dpa as a function of vacancy migration energy. The concentrations were calculated using the neutron irradiation conditions described in Table 3.1.

varied our model for 800H with vacancy migration energies of 0.9 to 1.5 eV for vacancies and 0.3, 0.5, and 0.7 eV for interstitials. Figures 3.8 and 3.9 show the final density of vacancy and interstitial faulted loops as a function of vacancy migration energy for a interstitial migration energy of 0.7 eV. We see that as vacancy migration energy increases, the densities of both faulted loops increase. This is due to the reduced mobility of the vacancies, caused by increasing vacancy migration energy, slowing the rates of all reactions of mobile vacancies with other defects and sinks. This slowing down of reactions effects the loss of vacancies to sinks significantly for high temperatures, causing the large increases in vacancy loop density for 650°C at 1.1 eV and 550°C at 1.4 eV. We do see a gradual increase in interstitial loops densities since the rate of recombination of vacancies to the interstitial loops is decreased, leaving more interstitials clusters intact.

When comparing the difference in densities between the different interstitial migration energy, the change was essentially insignificant for all values. When comparing 0.3 eV and 0.7 eV for intersititial migration energy, the results would only differ past the 5th significant digit. This is surprising since 70% of interstitials produced in cascade are in clusters small enough

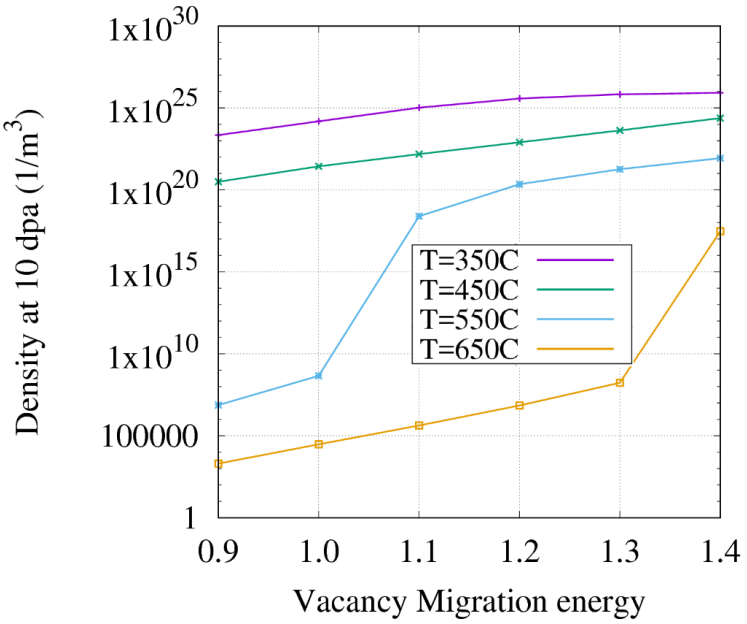

Figure 3.9: The concentration of vacancy faulted loops after 10 dpa as a function of vacancy migration energy. The concentrations were calculated using the neutron irradiation conditions described in Table 3.1.

to be considered mobile (not including perfect loops). One would expect that changing the migration energy of a such a large portion of the total defect would have some impact on the evolution of loops. This tells us that the interstitials that are created interact very quickly with other defects and sinks to the point where the change in the thermal dependence on mobility is minor. The dependence between vacancy migration energy and loop densities of both faulted loop types can predict reasonable loop densities at high temperatures. However, modifying the vacancy migration energy for an irradiation temperature of 350°C and 450°C still over predicts the densities of interstitial faulted loops by several orders of magnitudes.

Compared to the experimental data, we are seeing no trend towards saturation for the densities of either type of faulted loops under a wide range of sink strengths and migration energies. As dose increases, the loop densities approach unphysically high levels with no trend towards saturation. These increasing densities are accompanied with stagnant average interstitial Frank loop diameters that do not change with the range of parameters we chose. This leads us to conclude that the high densities are likely the result of excessive nucleation of loops directly through the g_i as opposed to a thermal process like the clustering of smaller defects into the loop group. Since this behavior is most evident in low temperature scenarios,

we set up a set of conditions that would determine if the generation of loops in cascade is truly the cause of the high loop densities.

3.2 MD Simulation Benchmark

Using the conditions specified in Table 3.1 under *MD Simulation Benchmark*, we tested if the high loop densities we were seeing in the neutron irradiation case were caused by the over nucleation of loops in the damage cascade. We modeled this scenario to provide comparison to several molecular dynamics studies ([34, 35]). These studies investigated the effects of a damage cascade occurring over the volume repeatedly, with 200 cascades in Ni-Fe alloys and 400 cascades in Ni-based solid-solution alloys respectively. As the number of cascades increases, the number of defects generated per cascade decreased until after ∼140 cascade the total number of defects in the simulation changed very little. We call the damage level where additional dose does not produce more defects the saturation level. These simulations show that at short timescales, the number of defects will tend toward some saturation level and not produce a high, linearly increasing defect density with increasing dose.

For comparing cluster dynamics to the MD simulations of Ref. [34], we calculated the PKA energy and the total time of the simulation to be equivalent to an extreme dose rate of 1.27×10^7dpa/s, using the NRT model, for a total of 5 nanoseconds [36]. We assumed a displacement energy for 800H of 40 eV and use the average number of Frenkel pairs created over the whole simulation versus the predicted amount for the production efficiency. As seen in Figure 3.10, when the MD Benchmark conditions were put into SPICES, the predicted number of defects significantly exceeded the saturation level observed in MD. If the dose levels were allowed to increase further, the number of defects, measured in parts per million, eventually exceeds 10^6. This trend occurred regardless of whether the defects were generated in loops or only in the mobile defect groups. Since the time scales are short and temperatures low, few if any reactions could take place and no recombination occurs. This can be seen by examining Figure 3.11 which shows the distribution of Frank loops at the end of the simulation. The increase in concentration for both faulted loop types match the production

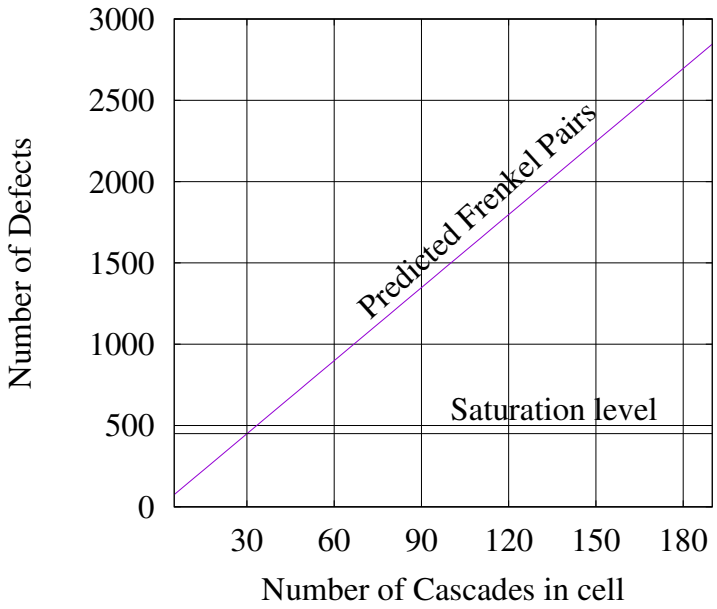

Figure 3.10: The predicted number of Frenkel pairs versus saturation defect number calculated in under MD Benchmark [34] conditions. The number of defects predicted quickly passes the saturation level from Ref. [34]

distribution identically, meaning any thermal interactions are negligible compared to the production of new loops directly in cascade.

The faulted loop populations in the neutron irradiation conditions have a similar unbounded growth. Instead of low temperatures and short timescales limiting the mobility of defects effectively stopping diffusion reactions, the faulted loops have no mobility by definition. The interstitial faulted loops, in particular, have strong thermal stability, as well as being immobile, meaning the interstitial Frank loops effectively trap the interstitials that compose the loop. Those interstitials have no way to react with other defects unless enough vacancies can recombine with the loop to effectively disassociate it into mobile interstitials. And since we are generating so many faulted loops directly in cascades, the vacancy flux that would go to shrink the loops and the interstitial flux that would go to grow the loops are diluted due to the large number of loops. Even though the reaction rate for faulted loops shrinking through recombination is heavily dependent on temperature, at lower temperatures the vacancy flux is to small to reduce the numbers significantly. Figure 3.10 demonstrates is

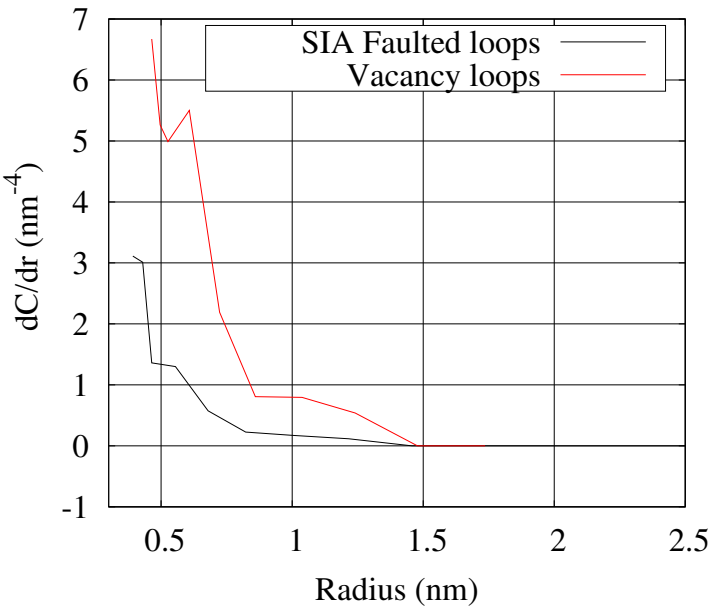

Figure 3.11: The distribution of interstitial and vacancy faulted loops at the end of the high dose rate simulation of 1.3×10^7 dpa/s to 0.065 dpa. The distribution is dominated by the production of the loops in cascade.

that we need some mechanism that operates at low temperatures that increases either the mobility of the faulted loops, or the mobility of the migrating defects.

3.3 Physical Mechanisms

Two possible physical mechanisms that could lead to the reduction of the number of loops present in the system are the the loops having an unfaulting reaction or that in the cascade volume itself there is enhanced recombination of defects that lead to a reduction in loop numbers. We investigate how these physical processes could be implemented in the current SPICES framework.

3.3.1 Unfaulting mechanism

As mentioned in section 2.1.1, in FCC metals it is possible for a Frank loop to transform into a perfect loop by interacting with a Shockley partial dislocation ($\vec{b} = \frac{a_0}{6}\langle 112 \rangle$). Depending on the Burgers vector of the Shockley partial and if the faulted loop is interstitial or vacancy

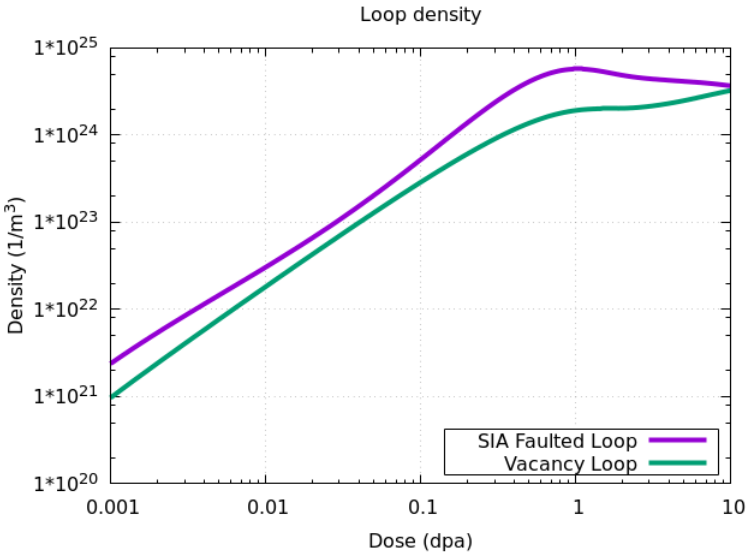

Figure 3.12: The density of both interstitial and vacancy faulted loops as a function of dose, under neutron irradiation conditions at 350°C. This is with a transformation rate equal to the dose rate and scales with loop area.

type, it can take more than one interaction of Shockley partials on Frank loops to turn them into perfect loops. This unfaulting reaction would lower Frank loops densities and effectively increase their mobility, since they would be transformed into mobile perfect loops. The interstitial that would otherwise be trapped in the faulted loop can then react with other defects, causing growth or shrinkage of different defects.

In SPICES, one can define a transformation rate from one defect class to another, as long as they have the same number of monomer components. We adjusted the parameters in equation 3.1 that define this rate so that k_n^* was the dose rate in dpa/s for $n = 1$. We also set $\phi = -1$ so that the rate scales with the area of the loop. The average loop diameter and density as a function of dose with this transformation mechanism of faulted to perfect loops are shown in Figures 3.12 and 3.13

$$k_n^* = \frac{\nu_0}{(|n|+1)^\phi} \exp\left[\frac{-E^*}{k_b T}\right] \tag{3.1}$$

Since the high number densities are most severe in the lower temperature simulation, only the 350°C results are shown. With the high unfaulting rate, we see that the number densities of both the faulted loop configuration do saturate. Around 1 dpa, both the interstitial and

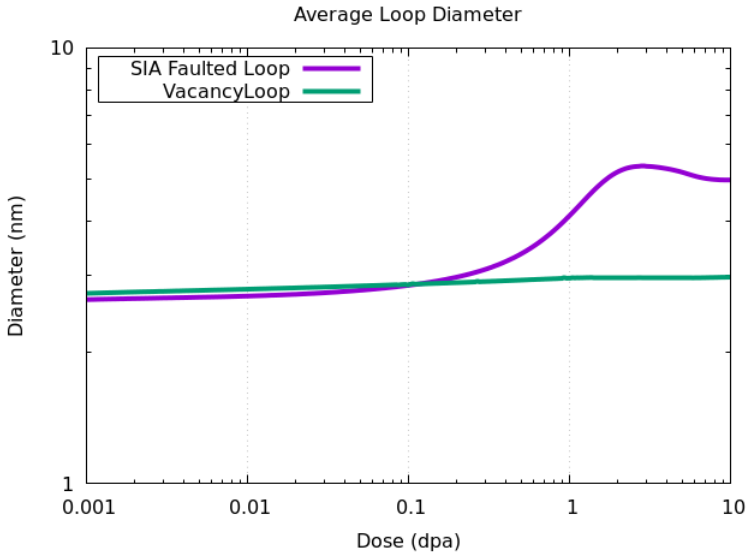

Figure 3.13: The diameter of both interstitial and vacancy faulted loops as a function of dose, under neutron irradiation conditions and 350°C. This is with a transformation rate equal to the dose rate and scales with loop area.

vacancy Frank loop densities level off. Both populations at that point had the generation of new faulted loops slowed significantly by the large number of extra perfect loops combining with them, either removing the loops entirely in the case of the vacancy loops or growing them significantly in the case of the interstitial Frank loops, as shown in Figure 3.13. Past 1 dpa, sink effects become significant in absorbing the extra perfect loops, causing an increase in vacancy loops. The sink effects also caused a reduction in average size and density for interstitial Frank loops, as the largest loops are more likely to transform into perfect loops. Unfortunately, even at the high transformation rate, the densities that both faulted loop populations arrive at is still much larger than the experimentally observed values for alloy 800H. We also observe some growth of interstitial loops as the unfaulting reaction becomes more significant. Even so, the transformation rate used is likely too high and a more realistic rate would have a smaller effect on the loop densities, and correspondingly not be able to decrease large densities shown in Figures 3.1 and 3.4.

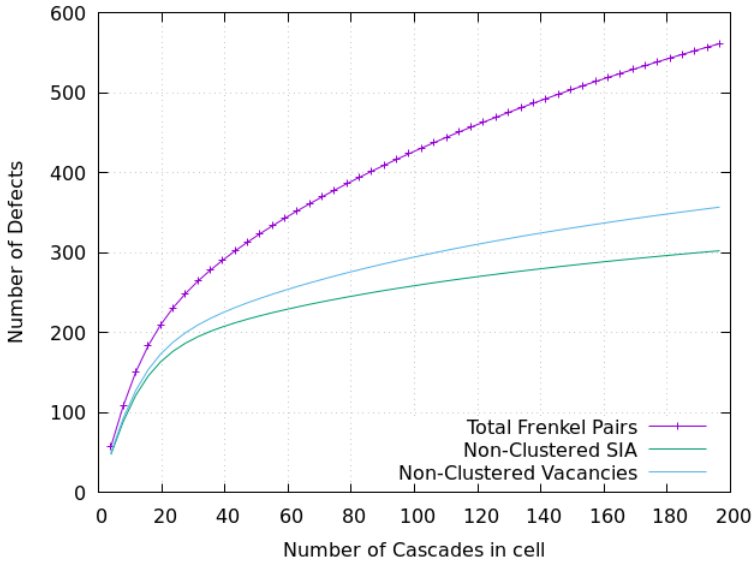

Figure 3.14: Total number of defects as a function of number of 20 keV cascades the addition of 50% of the defects created only react to recombine with loops. There does appear to be some saturation of small defects and loop populations as the dose increases.

3.3.2 Cascade Overlap Mechanism

The other physical process that could reduce the high number densities seen in the loop population is cascade driven recombination. As the damage cascades begin to overlap with defect clusters, the associated thermal spike either reconfigures the interstitials or vacancies of the overlapped cluster into a new cluster, or generates new interstitials or vacancies that then proceed to recombine with the original cluster. The effects of the overlap of cascade volumes with defect clusters is effectively athermal recombination and a reduction in defect production rate. Cascade driven recombination is an athermal effect that is at least one mechanism that would explain the discrepancy in Figure 3.10, and would reduce the faulted loop densities at low temperatures. We modeled this athermal effect by generating a new defect group along with the previous groups. We defined the new group as mobile vacancy and interstitials that are only allowed to recombine with preexisting defects and not grow any defect clusters. These recombination enhanced defects were given zero migration energy so that they would still recombine with other defects if the temperature was low, as in the MD Benchmark.

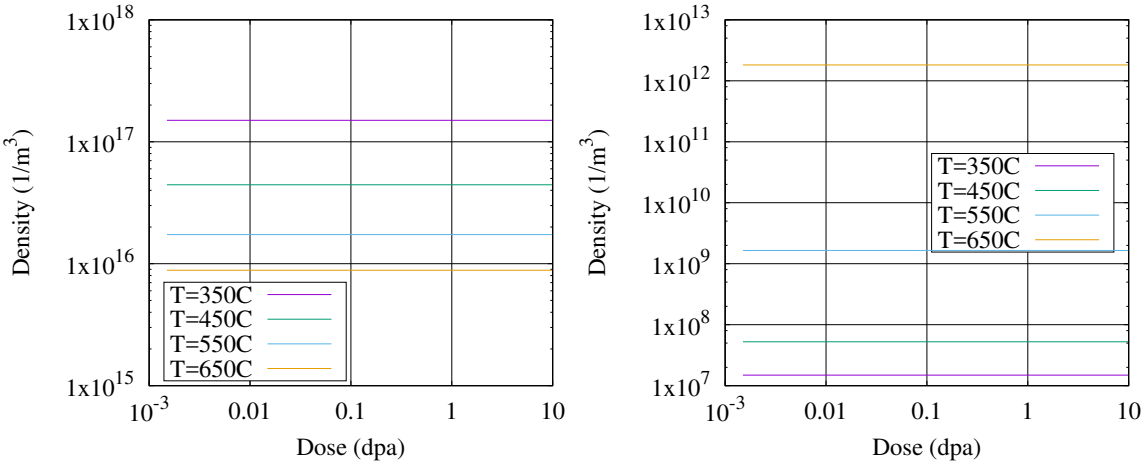

(a) Interstitial faulted loops

(b) Vacancy faulted loops

Figure 3.15: The density of faulted loops with increasing dose for the neutron irradiated condition with the addition of 50% of the defects created only react to recombine with loops.

Figure 3.14 show the results for the MD Benchmark conditions where 50% of the defects produced were preferentially recombined with existing defects (fraction ϵ). At ϵ=0.5, the increase in number of defects does decrease in a similar manner to the MD simulations we investigated, with a quick increase in damage at low doses and a lowering of the effective production rate with increasing dose.

Applying the same modifications to the neutron irradiated case were not as successful. For the lower dose rate with ϵ=0.5, shown in Figure 3.15, the densities of the interstitial and vacancy Frank loops were at steady state at the start of the simulation, and did not change with increasing dose. However, the loop densities were significantly decreased relative to the initital results of Figures 3.1 and 3.4. For the vacancy loops, we see the unusual behavior of number density increase as temperature increases, the opposite trend of what we have observed thus far. This is likely due to the modified defects recombining less with the evaporating vacancies, leading to more loops being nucleated from vacancy-vacancy interactions. The high ϵ for the neutron irradiated case is not appropriate for the low dose rate since effects of cascade driven recombination are only applicable for high defect concentrations. So, ϵ was lowered to 1% so that the cascade effects would not dominate the diffusion interactions at low defect concentration.

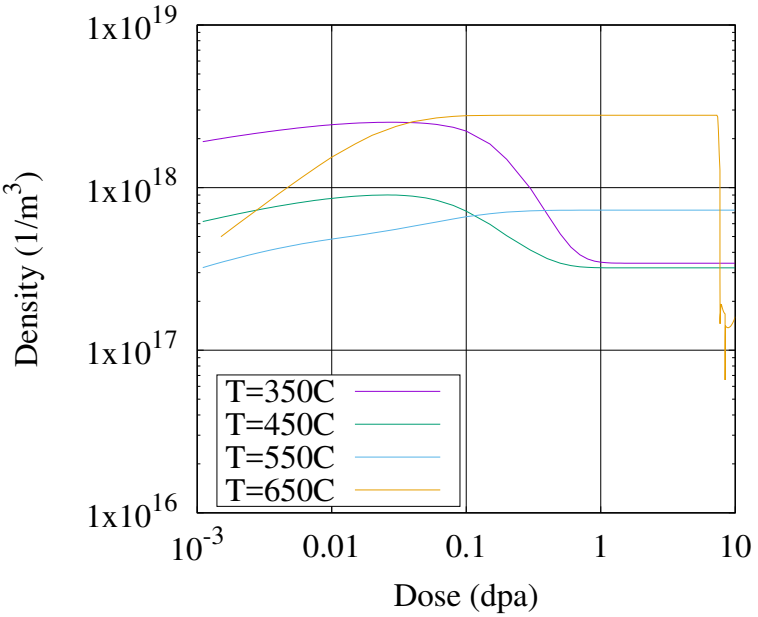

Figure 3.16: The density of interstitial faulted loops with increasing dose for the neutron irradiated condition with the addition of 1% of the defects created only react to recombine with loops.

Figure 3.16 shows the interstitial-type faulted loop density as a function of irradiation dose and temperature using the epsilon value of 1% to account for athermal cascade-induced defect overlap and recombination. The faulted interstitial loops, shown in Figure 3.16, are at a lower density compared to the initial results presented in Fig. 3.4. The athermal effects of the enhanced recombination are always active in the model, and this results in reducing the temperature dependence some of the thermal effects that would grow or shrink loops. Normally, the dissolution of the vacancy type loops significantly impacts the densities of the interstitial faulted loop, but the modified defects combine with a large portion of those freed vacancies, causing higher densities of interstitial Frank loops then compared to lower temperatures. If the cascade effects occurred before the concentration of defects becomes high enough, we are introducing an extra recombination term that reduced the densities and sizes of defects well below what they would be otherwise. This is clearly undesirable in modeling the evolution of the microstructure of alloy 800H and results generally in an under prediction of damage accumulation.

Another issues is that the final concentration is highly dependent on what value of ϵ is chosen. While there are promising results from Figure 3.14, a more rigorous definition of the critical dose and ϵ is required in order to properly apply similar modifications to the neutron irradiated case.

Chapter 4

Discussion and Future Work

Of the two possible physical mechanisms considered in Chapter 3 that could provide a physically-based model to eliminate the unphysically high densities predicted in our model, the unfaulting reaction mechanism is not deemed to be the solution for two reasons. One is that in order for the unfaulting mechanism to take place, faulted loops need to grow in size to increase the favorability of the unfaulting reaction to occur. From Ref. [26], the reaction is favorable if the following equation is satisfied:

$$\gamma > \frac{Ga^2}{24\pi r_{\text{loop}}} \frac{2-\nu}{1-\nu} \ln\left(\frac{2r_{\text{loop}}}{r_o}\right) \tag{4.1}$$

Where r_{loop} is the radius of the loop, G is the shear modulus, ν is the Poisson ratio, a is the lattice parameter, r_o is the dislocation core radius, and γ is the stacking fault energy. Equation 4.1 is based on when a perfect loop is energetically favorable compared to a Frank loop, with its extra stacking fault energy, but smaller Burgers vector magnitude. Using the parameters for 800H at 350°C, the critical loop radius above which this reaction is favorable is more than 20 nm, much greater than the size of most of the interstitial loops we predict in our model. This calculation only describes when the unfaulting reaction would be energetically favorable, and does not include that the Shockley partials would need to nucleate somewhere in the loop in order for the reaction to occur. The other reason is that at lower temperatures, like under the MD Benchmark conditions, the model would still fail to predict the saturation of defect densities. Even if all the faulted loops transform into a

glissile configuration, the temperatures would be too low and the timescales too short for the perfect loops to react with other defects. While the addition of the Shockley partial mechanism likely would make the model more physically realistic, in most of the conditions that we wish to model, the faulted loops do not grow to the size required to impact the predictions significantly.

The cascade overlap mechanism is thus deemed to be more promising and more effective in reducing the high number densities since the additional recombination occurs as an athermal process. The two main issues with the implementation we have preformed thus far is that the effects of cascade induced recombination occur regardless of the concentrations of defects, and that the one could chose an ϵ to get whatever desired behavior required. For the model to represent the cascade effects appropriately, a more rigorous derivation and implementation is necessary to generalize the solution. We would need to formalize how to choose an appropriate ϵ and when to include the additional recombination and scaled defect production. Instead of modeling the enhanced recombination as a set of additional defect types, we plan on adding the extra recombination as an additional reaction rate constant that appropriately treats recombination and the production of new smaller clusters following incomplete annihilation or recombination events induced by cascade overlap. Currently, the defect-defect interactions are calculated through the reaction network described in equation 2.2. Normally in cluster dynamics, the actual change in concentration from those reactions is proportional to the concentration of each defect (C_i,C_j), and a reaction rate constant that depends on the mobility of the defect at the current temperature. At sufficiently low temperatures, the only term left in the equation 2.1 is the generation term, causing the unbounded growth in concentrations. The additional reaction term we wish to add that represents the enhanced recombination needs to be athermal, so that at low temperatures we get the defect saturation shown in Ref. [34, 35]. This means that the rate at which the reaction occurs does not relate to the diffusivity of the defects, but on the rate at which a cascade volume will overlap with a defect.

As an approximation for the gradual cascade effects, an additional athermal set of reactions can be added to the reaction network that behave similarly to additional recombination and production scaling. One possibility is described in equations and equation

4.2 for loops and for spherical geometries4.3.

$$R_{i+j}\Big|_{\text{overlap}} = \frac{1}{\sum_k \pi(r_k + a_0)^2 |b_k| C_k} \pi(r_j + a_0)^2 |b_j| \dot{C}_i C_j \tag{4.2}$$

$$R_{i+j}\Big|_{\text{overlap}} = \frac{1}{\sum_k \frac{4\pi}{3}(r_j + a_0)^3 C_k} \frac{4\pi}{3}(r_j + a_0)^3 \dot{C}_i C_j \tag{4.3}$$

For both equations 4.2 and 4.3, $R_{i+j}|_{\text{overlap}}$ represents the overlap reaction rate contribution for each defect cluster concentration of size j recombining with the modified defects i. $\dot{C}_i$ represents the concentration of modified defects generated per unit time or the cascade induced recombinations density per unit time. The overlap reaction rate depends on the volume of each defect cluster j, because the increase in defect size will increase the probability of cascade overlap. The volume of a defect loop is $\pi(r_j + a_0)^2|b_j|$ where r_j is the radius of the loop, a_0 is the lattice parameter, and $|b_j|$ is the magnitude of the loops Burgers vector. Both overlap reaction rate eqautions are divided by a normalization term, that is the summation of the defect cluster concentrations C_k multiplied by the associated defect volume. This normalization controls the enhanced recombination by not allowing the number of defects that are removed through the cascade effects to exceed the total number of defects. At some critical dose when the cascade overlap terms become significant, these additional terms are included in the calculation, as well as a term to scale the cascade production term such that mass is conserved. Each cluster size would have two of these summation terms, one that subtracts out of the group represent the recombination into a smaller defect, and a positive term that represents large defects undergoing partial annihilation or recombination leading to a smaller cluster in that group. The main unknowns in the additional terms is the critical dose that activates the additional cascade recombination terms and the $\dot{C}_i$ terms.

In order to find the appropriate values of $\dot{C}_i$ and the critical dose to start including the modifications, we plan on performing molecular dynamics simulations. Similar to previous work investigating the effects of overlapping cascade volumes ([34, 35]), we will simulate the effects of a cascade impacting the same volume repeatedly. Using copper as a surrogate (with the interatomic potential for Cu described in Ref. [37]), each cascade we will track the number of isolated point defects, as well as the full size dependent

cluster populations of interstitial and vacancy type. With this information, we will be able to calculate the critical dose by finding when the when the defect evolution deviates substantially from cluster dynamics model predictions without incorporating cascade overlap based recombination. The $\dot{C}_i$ term would be associated the volumetric generation required to match the reduced generation of defects. With the inclusion of the critical dose activation of cascade-induced recombination effects and matching the reduction of defect concentration to an MD simulation, the effects should be similar to the implementation of cascade effects in section 3.3.2 but with more realistic terms and application in the cluster evolution.

4.1 Summary

In using cluster dynamics to model alloy 800H microstructure as a function of dose and temperature, we predict very large faulted loop densities, orders of magnitude larger than experiments under similar conditions. Intrinsic sink strength and defect migration energy were varied to see if the high densities were caused by improperly choosing those parameters, but these variations had little to no effect on decreasing the densities for both interstitial and vacancy faulted loops. We have come to the conclusion that cluster dynamics, while excellent when species are mobile, needs modifications when the directly produced defects are immobile. The source of our high densities are from generating a large number of immobile, thermally stable faulted loops directly in cascade. The number density of the faulted loops quickly grows to the level where the flux of mobile vacancies isn't enough to counteract the nucleation of new loops, and the number densities grow without bound. The physical process that would reduce the large number densities of small faulted loops is the thermal spike during a damage cascade which enhances recombination, regardless of environmental temperatures.

This enhanced recombination causes the production of the defect to slow at high defect concentration. To approximate this recombination and changing defect production in cluster dynamics, we propose an additional set of reaction terms that instead of representing a C_i-C_j reaction, represents a C_i-g_j reaction. This term will activate after some critical dose, so that the effects of the cascade enhanced recombination only becomes relevant when the

probability of a damage cascade overlapping with some preexisting defect is sufficiently high. In order to find the proper values of the critical dose and $\dot{C}_i$ terms, molecular dynamics simulations are required to fit the parameters to realistic cascade-enhanced recombination rates. Once the parameters are calculated, applying the athermal cascade effects will produce more realistic results that will better predict the microstructures seen in experiments. Adding these athermal reaction terms, while critical for modeling Alloy 800H, will be important for modeling other austenitic alloys since they will likely have similar stacking fault energies and microstructure behavior. Once the experiment can be matched with application of the additional cascade mechanism, the model can be extended to predict how alloy 800H would predict under the wide range of temperatures and doses that the alloy is expected to experience in Generation IV nuclear reactors.

Bibliography

[1] Nuclear Energy Agency International Energy Agency. *IEA/NEA Technology Roadmap: Nuclear Energy*. Nuclear Energy Agency, 2015.

[2] International Atomic Energy Agency. *Nuclear Power Reactors in the World*. Number 2 in Reference Data Series. International Atomic Energy Agency, Vienna, 2017.

[3] Robert Youngblood. *Objective 1: Extend Life, Improve Performance, and Maintain Safety of the Current Fleet Implementation Plan*. Idaho National Laboratory, 2011.

[4] Edward A. Kenik and Jeremy T. Busby. Radiation-induced degradation of stainless steel light water reactor internals. *Materials Science and Engineering: R: Reports*, 73 (7):67 – 83, 2012.

[5] S.J. Zinkle and L.L. Snead. Designing radiation resistance in materials for fusion energy. *Annual Review of Materials Research*, 44(1):241–267, 2014.

[6] S.J. Zinkle and G.S. Was. Materials challenges in nuclear energy. *Acta Materialia*, 61 (3):735 – 758, 2013.

[7] H. R. Brager, J. L. Straalsund, J. J. Holmes, and J. F. Bates. Irradiation-produced defects in austenitic stainless steel. *Metallurgical Transactions*, 2(7):1893–1904, Jul 1971.

[8] S.J. Zinkle, P.J. Maziasz, and R.E. Stoller. Dose dependence of the microstructural evolution in neutron-irradiated austenitic stainless steel. *Journal of Nuclear Materials*, 206(2):266 – 286, 1993.

[9] C Pokor, Y Brechet, P Dubuisson, J.-P Massoud, and A Barbu. Irradiation damage in 304 and 316 stainless steels: experimental investigation and modeling. part I: Evolution of the microstructure. *Journal of Nuclear Materials*, 326(1):19 – 29, 2004.

[10] B. Weiss and R. Stickler. Phase instabilities during high temperature exposure of 316 austenitic stainless steel. *Metallurgical Transactions*, 3(4):851–866, Apr 1972.

[11] D. Hull and D.J. Bacon. 10 - Strength of Crystalline Solids. In D. Hull, , and D.J. Bacon, editors, *Introduction to Dislocations (Fourth Edition)*, pages 193 – 236. Butterworth-Heinemann, Oxford, fourth edition edition, 2001.

[12] L. K. Mansur. Theoretical evaluation of a mechanism of precipitate-enhanced cavity swelling during irradiation. *Philosophical Magazine A*, 44(4):867–877, 1981.

[13] A.F. Rowcliffe, L.K. Mansur, D.T. Hoelzer, and R.K. Nanstad. Perspectives on radiation effects in nickel-base alloys for applications in advanced reactors. *Journal of Nuclear Materials*, 392(2):341 – 352, 2009.

[14] Special Metals Corporation number =. Alloy 800 technical report.

[15] Bruce A. Hilton Jian Gan, PhD. *TEM Examination of Advanced Alloys Irradiated in ATR*. Sep 2007.

[16] J. Gan, J.I. Cole, T.R. Allen, S. Shutthanandan, and S. Thevuthasan. Irradiated microstructure of alloy 800h. *Journal of Nuclear Materials*, 351(1):223 – 227, 2006. Proceedings of the Symposium on Microstructural Processes in Irradiated Materials.

[17] L. Tan, K. Sridharan, and T.R. Allen. The effect of grain boundary engineering on the oxidation behavior of incoloy alloy 800h in supercritical water. *Journal of Nuclear Materials*, 348(3):263 – 271, 2006.

[18] L. Tan, K. Sridharan, T.R. Allen, R.K. Nanstad, and D.A. McClintock. Microstructure tailoring for property improvements by grain boundary engineering. *Journal of Nuclear Materials*, 374(1):270 – 280, 2008.

[19] D.S. Gelles. Microstructural examination of several commercial alloys neutron irradiated to 100 dpa. *Journal of Nuclear Materials*, 148(2):136 – 144, 1987.

[20] Frank Garner and H R. Brager. Swelling of austenitic fe-ni-cr ternary alloys during fast neutron irradiation. 11 2017.

[21] L. Tan, J.T. Busby, H.J.M. Chichester, K. Sridharan, and T.R. Allen. Thermomechanical treatment for improved neutron irradiation resistance of austenitic alloy (fe21cr32ni). *Journal of Nuclear Materials*, 437(1):70 – 74, 2013.

[22] Rudolf Sizmann. The effect of radiation upon diffusion in metals. *Journal of Nuclear Materials*, 69-70(Supplement C):386 – 412, 1978.

[23] A. Hardouin Duparc, C. Moingeon, N. Smetniansky de Grande, and A. Barbu. Microstructure modelling of ferritic alloys under high flux 1 mev electron irradiations. *Journal of Nuclear Materials*, 302(2):143 – 155, 2002.

[24] Aaron A Kohnert and Brian D Wirth. Grouping techniques for large-scale cluster dynamics simulations of reaction diffusion processes. *Modelling and Simulation in Materials Science and Engineering*, 25(1):015008, 2017.

[25] MV Smoluchowski. Mathematical theory of the kinetics of the coagulation of colloidal solutions. *Z. Phys. Chem.*, 92:129–168, 1917.

[26] D. Hull and D.J. Bacon. 5 - Dislocations in Face-centred Cubic Metals. In D. Hull, , and D.J. Bacon, editors, *Introduction to Dislocations (Fourth Edition)*, pages 82 – 101. Butterworth-Heinemann, Oxford, fourth edition edition, 2001.

[27] S.J. Zinkle and R.L. Sindelar. Defect microstructures in neutron-irradiated copper and stainless steel. 155-157:1196–1200, 07 1988.

[28] S.J. Zinkle, L E. Seitzman, and W G. Wolfer. Stability of vacancy clusters in metals I: Energy calculations for pure metals. 55:111–125, 01 1987.

[29] J. Brillo and I. Egry. Surface tension of nickel, copper, iron and their binary alloys. *Journal of Materials Science*, 40(9):2213–2216, May 2005.

[30] R. E. Schramm and R. P. Reed. Stacking fault energies of seven commercial austenitic stainless steels. *Metallurgical Transactions A*, 6(7):1345, Jul 1975.

[31] Raymond E. Schramm and Richard P. Reed. Stacking fault energies of fcc fe-ni alloys by x-ray diffraction line profile analysis. *Metallurgical Transactions A*, 7(3):359–363, Mar 1976.

[32] Cecil G. Rhodes and Anthony W. Thompson. The composition dependence of stacking fault energy in austenitic stainless steels. *Metallurgical Transactions A*, 8(12):1901–1906, Dec 1977.

[33] D.J Bacon, Yu.N Osetsky, R Stoller, and R.E Voskoboinikov. MD description of damage production in displacement cascades in copper and α-iron. *Journal of Nuclear Materials*, 323(2):152 – 162, 2003.

[34] K Vörtler, N Juslin, G Bonny, L Malerba, and K Nordlund. The effect of prolonged irradiation on defect production and ordering in Fe–Cr and Fe-Ni alloys. *Journal of Physics: Condensed Matter*, 23(35):355007, 2011.

[35] Mohammad W. Ullah, Dilpuneet S. Aidhy, Yanwen Zhang, and William J. Weber. Damage accumulation in ion-irradiated Ni-based concentrated solid-solution alloys. *Acta Materialia*, 109:17 – 22, 2016.

[36] M.J. Norgett, M.T. Robinson, and I.M. Torrens. A proposed method of calculating displacement dose rates. *Nuclear Engineering and Design*, 33(1):50 – 54, 1975.

[37] Y. Mishin, M. J. Mehl, D. A. Papaconstantopoulos, A. F. Voter, and J. D. Kress. Structural stability and lattice defects in copper: Ab initio, tight-binding, and embedded-atom calculations. *Phys. Rev. B*, 63:224106, May 2001.

Vita

Andrew Nicholas Payant was born in Menomonee Falls, Wisconsin to John Payant and Dobra Payant. He attended Waukesha West High School, and graduated from the University of Minnesota: Twin Cities with a Bachelors of Science in Physics and Astrophysics in 2016. He then continued to The University of Tennessee and accepted a Graduate Research Assistant position on August 2016. Andrew will earn a Masters of Science degree in Nuclear Engineering in December of 2017.